

# Mesoscopic Interaction Potential for Carbon Nanotubes of Arbitrary Length and Orientation<sup>†</sup>

Alexey N. Volkov and Leonid V. Zhigilei\*

University of Virginia, Department of Materials Science and Engineering, 395 McCormick Road, Charlottesville, Virginia 22904-4745

Received: June 30, 2009; Revised Manuscript Received: August 24, 2009

Mesoscopic tubular potential is developed for the description of the van der Waals interaction between straight single-walled carbon nanotubes (CNTs) of arbitrary length and orientation. The potential is formulated within a general continuum description of the van der Waals intertube interactions based on the integration of an interatomic potential over the surfaces of the interacting nanotubes. The tubular potential reduces the functional dependence of the potential energy of the interacting nanotubes on six independent geometric variables to a combination of several functions, each depending on only one or two geometric parameters. The parametrization of the tubular potential is based on the carbon–carbon interatomic potential describing nonbonding interactions in graphitic structures. An application of the tubular potential for analytical analysis of the interaction between two CNTs reveals the conditions and driving forces responsible for the alignment of nanotubes and generation of CNT bundles. First mesoscopic simulations, performed with the tubular potential for a system consisting of thousands of nanotubes and having dimensions on the order of a micrometer, predict a spontaneous self-assembly of nanotubes into a continuous network of bundles with partial hexagonal ordering of CNTs in the bundles. The structures produced in the simulations are similar to the structures of CNT films and mats observed in experiments. The general procedure used in the design of the tubular potential is not limited to single-walled CNTs or other graphitic structures and can be extended to a diverse range of systems consisting of various types of nano- and microtubular elements, such as nanotubes, nanorodes, and microfibers, providing new opportunities for mesoscopic modeling of complex nanocomposite materials.

## 1. Introduction

A principal challenge in the computational investigation of a broad class of nanomaterials and nanoscale devices based on carbon nanotubes (CNTs) is presented by the absence of a computationally efficient description of the effective van der Waals interactions among the CNTs. These weak nonbonding interactions are responsible for the spontaneous self-organization of CNTs into complex intertwined structures consisting of interconnected bundles or ropes of nanotubes, such as the ones observed in CNT films, mats, and fibers; see, e.g., refs 1–10. The microscopic structure of CNT-based materials is defined by the spatial arrangement of CNT bundles rather than nanotubes themselves, and therefore, a computational analysis of the structure and properties of these materials should include a large number of CNTs. While a number of computationally efficient mesoscopic models for simulation of individual CNTs have been developed,<sup>11–14</sup> the lack of a correspondingly efficient and accurate description of intertube interactions prevents application of these models for investigation of structural self-organization and collective dynamic behavior in CNT-based materials and structures.

In atomistic simulations, the van der Waals interactions among single-walled CNTs<sup>15–19</sup> or between individual shells in multiwalled CNTs<sup>15,19</sup> are computed through the summation of the corresponding energies and forces for all pairs of interacting atoms. The interatomic potential for the nonbonding van der Waals interactions is typically taken in the form of the

Lennard-Jones potential, with parameters fitted to some of the properties of graphite.<sup>20,21</sup> The atomistic modeling, however, is computationally expensive and cannot be applied for investigation of the dynamic behavior of large groups of CNTs. The systems used in atomistic simulations have been limited to small bundles consisting of several (e.g., four,<sup>19</sup> six,<sup>16</sup> or seven<sup>17,18</sup>) very short (from nanometers to tens of nanometers) single-walled CNTs or individual multiwalled CNTs consisting of several (e.g., four<sup>19</sup> or eight<sup>15</sup>) shells.

A continuum representation of the van der Waals interactions based on numerical integration over the surfaces of interacting CNTs has been developed within a continuum mechanics model constructed based on interatomic interactions.<sup>14,22,23</sup> Although more efficient than the atomistic simulations, the finite element implementation of this continuum model includes a large number of nodes and exhibits only a moderate improvement in the computational efficiency as compared to the atomistic approach.<sup>22</sup> Indeed, the number of quadrature points necessary for an accurate representation of van der Waals interactions in a 40-walled 480 nm long CNT is found to be 10 million, only 3 times less than the number of atoms in this system, 31 million.<sup>14</sup>

Neither summation of interatomic interactions in atomistic simulations nor the direct numerical integration over the surfaces of interacting nanotubes can provide a method for evaluation of the van der Waals interactions that would be sufficiently fast to enable mesoscopic simulations of large CNT ensembles. A promising approach for an efficient description of van der Waals interactions in graphitic systems has been suggested in a series of works demonstrating that simple effective/mesoscopic po-

<sup>†</sup> Part of the “Barbara J. Garrison Festschrift”.

\*Author to whom correspondence should be addressed. E-mail: lz2n@virginia.edu.

tentials can be obtained within a continuum approach, where the summation of interatomic interactions is approximated by the integration over the surfaces of interacting objects.<sup>24–30</sup> The effective potentials have been derived for interactions between fullerene molecules,<sup>24</sup> a fullerene molecule and a graphene sheet,<sup>25,26</sup> a fullerene and a single-walled CNT,<sup>26</sup> a molecule or a gas-phase atom and a CNT,<sup>29</sup> a CNT and a surrounding polymer material,<sup>30</sup> single-walled CNTs of the same<sup>26</sup> and different radii,<sup>27</sup> and multiwalled CNTs of different radii.<sup>28</sup> The effective potentials describe the nonbonding interactions between the graphitic structures at a mesoscopic rather than atomistic level, expressing the interaction energies in the form of simple functions that depend only on the distance between interacting objects. Moreover, when expressed in terms of reduced parameters, the interactions derived for different graphitic structures are found to be well represented by a universal graphitic potential.<sup>26–28</sup> While the effective mesoscopic potential for fullerene molecules and graphene have already found applications in large-scale mesoscopic simulations of fullerene films, clusters, and bulk structures, e.g., refs 24 and 31–33, the application of the potential for CNTs is limited by the geometrical limitations of the models—all derivations have been performed for straight, infinitely long, parallel CNTs.<sup>26–28</sup> The only CNT systems that can be investigated with the current models are bundles of straight infinitely long nanotubes.<sup>26,29,34,35</sup>

In order to enable mesoscopic simulations of a variety of CNT materials with complex spatial arrangement of nanotubes, in this paper, the continuum approach for calculation of the mesoscopic potential is extended to the interactions between CNTs of arbitrary lengths and orientation. In spite of the geometrical complexity of the problem (the interaction energy is a function of six independent geometric variables), a compact and accurate approximation of the interaction potential is established and verified for various CNT configurations. The developed mesoscopic potential is applied for analysis of the torque acting on nonparallel CNTs and responsible for self-assembly of CNTs into bundles. The applicability of the potential for large-scale dynamic mesoscopic simulations of the collective behavior of large CNT ensembles is also illustrated in a simulation performed for a system consisting of 4050 (10,10) 400 nm long single-walled CNTs.

## 2. Mesoscopic Tubular Potential for the van der Waals Interaction between CNTs

In this section, we introduce an effective/mesoscopic tubular potential that provides an approximate but highly accurate description of nonbonding interactions between two straight single-walled CNTs of arbitrary length and relative orientation. The tubular potential expresses the intertube interaction energies and forces in a compact functional form that is suitable for computationally efficient implementation in a dynamic model that is capable of treating large ensembles of interacting CNTs. Although the tubular potential is appropriate for analysis of systems consisting of straight CNTs (e.g., section 3), we envision that the main area of future applications of the potential will be in modeling of the dynamic behavior of large ensembles of flexible CNTs represented as chains of cylindrical segments (e.g., section 4). Therefore, below, we use the term “CNT segment” to refer to one of the main structural elements considered in this work—a straight CNT of a finite length.

**2.1. From Atomistic to Continuum Description of CNT–CNT Interaction.** The mesoscopic tubular potential describing the van der Waals interaction between two straight single-walled CNTs (or CNT segments) is designed in this work within a

continuum approach based on the integration over the surfaces of the interacting CNTs.<sup>14,22–30</sup> It is convenient, however, to make a direct connection between the continuum approach and atomistic representation of the van der Waals interactions. In atomistic modeling, the nonbonding interaction between CNTs is represented by a sum of interatomic interactions for all pairs of carbon atoms that belong to different CNTs. The nonbonding interatomic interactions are commonly described by the Lennard-Jones potential modified by a cutoff function that enforces the finite range of the interatomic interactions:

$$\varphi(r) = 4\epsilon \left[ \left( \frac{\sigma}{r} \right)^{12} - \left( \frac{\sigma}{r} \right)^6 \right] C(r) \quad (1)$$

where  $r$  is the distance between the interacting atoms,  $\epsilon$  and  $\sigma$  are parameters of the potential that define the energy and length scales of the carbon–carbon interaction, respectively, and  $C(r)$  is the cutoff function. The values of the parameters of the potential are typically obtained by fitting to the structural, cohesive, and/or elastic properties of various carbon systems, with values obtained for graphite and CNTs exhibiting a substantial deviation from those providing the best fit to fullerene systems.<sup>26</sup>

In this work, the functional form of the cutoff function and the parameters of the potential are adopted from a popular AIREBO potential,<sup>21</sup> commonly used in atomistic modeling of carbon nanostructures and molecular hydrocarbon systems; see, e.g., refs 36–38. The values of  $\sigma = 3.40$  Å and  $\epsilon = 2.84$  meV are chosen in this case to reproduce the interlayer separation and the elastic constant  $c_{33}$  in graphite. The cutoff function is defined as  $C(r) = S(\tau(r))$ , where

$$S(\tau) = H(-\tau) + H(\tau)H(1 - \tau)[1 - \tau^2(3 - 2\tau)] \quad (2)$$

$\tau(r) = (r - r_{c0})/(r_c - r_{c0})$ , and  $H(\tau)$  is the Heaviside step function. The cutoff function varies from 1 to 0 when  $r$  changes from  $r_{c0}$  to  $r_c$ , which ensures a smooth transition of the interatomic potential to zero at the cutoff distance  $r_c$ . The values of the cutoff parameters are  $r_{c0} = 2.16\sigma$  and  $r_c = 3\sigma$ .<sup>39</sup>

The relative position of two straight CNTs (or CNT segments) can be characterized by six independent geometric parameters, as illustrated in Figure 1a. The relative position of the axes of the segments is defined by the shortest distance  $h$  and the angle  $\alpha$  between the axes. The length and the location of the segments along the axes are defined by coordinates of their ends,  $\xi_1$ ,  $\xi_2$ ,  $\eta_1$ , and  $\eta_2$  with respect to the points defining the shortest distance between the axes,  $O$  and  $O'$ . In order to simplify further discussion, we assume that the directions of axis  $O\xi$  and  $O'\eta$  are chosen so that the conditions  $|\xi_1| \leq \xi_2$  and  $|\eta_1| \leq \eta_2$  are satisfied. These conditions imply, in particular, that if both ends of a CNT segment are located on the same side of its axis from point  $O$  (or  $O'$ ), the axis is directed toward the segment and the first end of the segment is closer to the point of origin of the axis than the second end. The lengths of the segments can be finite, semi-infinite, or infinite. In latter cases, some of the coordinates,  $\xi_1$ ,  $\xi_2$ ,  $\eta_1$ , and  $\eta_2$ , can have infinite values.

Following an approach adopted in refs 24–28 for the design of the effective/mesoscopic potentials for infinitely long parallel CNTs, fullerenes, and graphene sheets, the design and parameterization of the mesoscopic tubular potential for CNT segments of arbitrary length and orientation is based on the substitution of summation of interatomic interactions by integration over

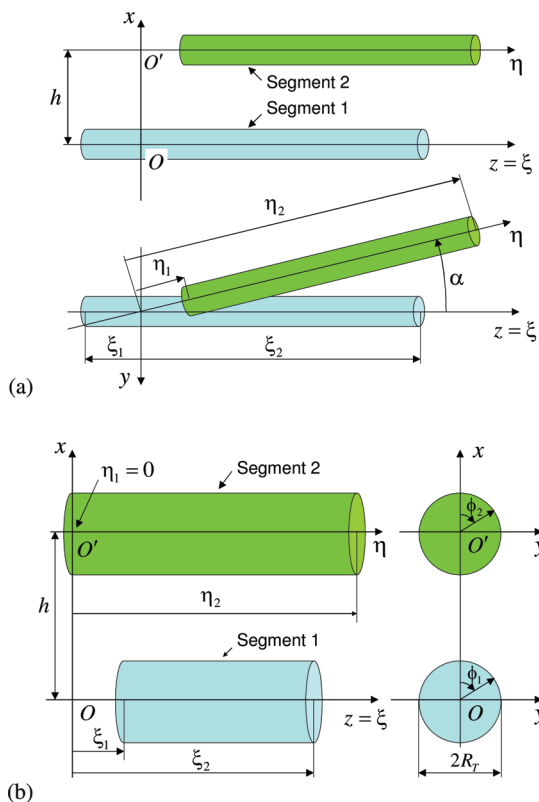


**Figure 1.** Schematic sketch illustrating the introduction of local coordinates  $Oxyz$  and geometrical parameters used for characterization of the relative positions of two nonparallel (a) and parallel (b) straight cylindrical CNT segments. The side and top views are shown in panel a; only the side view is shown in panel b. In panel a, the axis  $x$  is directed along the vector  $\vec{OO'}$  defining the shortest distance between the axes of the segments. In panel b, for the convenience of the analysis presented in section 2.3, the origin of the Cartesian coordinates is chosen so that the axis  $Ox$  goes through the left end of the second segment ( $\eta_1 = 0$ ). Cross sections of the segments are shown in panel b, with angles  $\phi_1$  and  $\phi_2$  specifying positions of points in the cross sections used for integration over the surfaces of the two segments.

the surfaces of the interacting nanotubes. The real atomic configurations at the surfaces of CNTs are replaced in this case by an average continuous distribution of atoms with surface density  $n_\sigma$ , so that the segment–segment interaction potential  $U_{SS}$  can be found by integration of the interatomic potential over the surfaces of the interacting segments. For two CNT segments of the same radius  $R_T$ , the interaction potential can then be expressed as

$$U_{SS}(h, \alpha, \xi_1, \xi_2, \eta_1, \eta_2) = n_\sigma^2 R_T^2 \int_{\xi_1}^{\xi_2} \int_0^{2\pi} \int_{\eta_1}^{\eta_2} \int_0^{2\pi} \varphi(r(h, \alpha, \xi, \phi_1, \eta, \phi_2)) d\phi_2 d\eta d\phi_1 d\xi \quad (3)$$

where the integration is performed along the axes of the segments,  $\xi$  and  $\eta$ , and over the angles  $\phi_1$  and  $\phi_2$  that specify positions of points in the cross sections of segments (see Figure 1b). The distance between two points on the surfaces of the segments is expressed through the six geometric parameters as

$$r(h, \alpha, \xi, \phi_1, \eta, \phi_2) = [(h + R_T(\cos \phi_2 - \cos \phi_1))^2 + (R_T(\sin \phi_2 \cos \alpha - \sin \phi_1) - \eta \sin \alpha)^2 + (R_T \sin \phi_2 \sin \alpha + \eta \cos \alpha - \xi)^2]^{1/2} \quad (4)$$

The integral for the segment–segment interaction potential, eq 3, is written under assumption that interacting segments have the same radius  $R_T$ . The distribution of radii in real CNT materials depends on the process used for material fabrication<sup>2,6,10,40</sup> but is often sufficiently narrow (e.g., the single-walled CNTs produced by laser ablation of carbon targets have an average radius of  $\sim 0.7$  nm<sup>1,2,6,40</sup> with variation of less than  $\pm 0.15$  nm<sup>2</sup>) to justify the assumption of a constant radius in modeling of such materials. The deviation from the perfect cylindrical shapes due to the van der Waals intertube interactions, particularly significant for single-walled CNTs of large diameters,<sup>15,41,42</sup> as well as changes in the shapes of the local cross sections due to the buckling or irreversible plastic deformation of nanotubes under compression, bending, and torsional deformation<sup>14,18,19,22,23,43</sup> are neglected in the model. CNTs are assumed to have ideal structure and geometry that is completely characterized by a pair of integer numbers  $(n,m)$  defining the chiral vector of a nanotube.<sup>44,45</sup> The radius of an  $(m,n)$  CNT can be calculated as  $R_T = l_c[3(n^2 + m^2 + nm)]^{1/2}/(2\pi)$ , where  $l_c = 1.421$  Å is the carbon–carbon interatomic distance in a graphene sheet.<sup>45</sup> The number density of atoms on the surface of a CNT is  $n_\sigma = 4/(3\sqrt{3}l_c^2) \approx 38.1$  nm<sup>-2</sup>. The presence of hemispherical caps at the ends of the nanotubes is not taken into account in the potential defined by eq 3 but can be added to the computational model implementing the mesoscopic tubular potential.

The four-dimensional integral defining the segment–segment potential, eq 3, can only be simplified<sup>26–28</sup> or expressed in terms of series expansions<sup>46</sup> for some special cases, e.g., for infinitely long parallel CNT and interatomic interaction described by the Lennard-Jones potential without a cutoff. In the general case of nonparallel nanotubes of finite lengths, the direct numerical integration of eq 3 is the only way to calculate the segment–segment interaction potential. An analysis of several test cases indicates, however, that an acceptable accuracy of the integration can be obtained only when a large number of quadrature points is used, e.g., 50–100 quadrature points per nm of a (10,10) CNT. While this number is smaller than the number of atoms ( $\sim 162$  atoms/nm for a (10,10) CNT), the computational cost of the integration is still too high to allow for “on the fly” evaluation of the van der Waals interactions in a dynamic simulation of large CNT ensembles. A similar observation on the high computational cost of the description of the van der Waals interactions has been made in continuum simulations of multiwalled CNTs in refs 14 and 22. The fact that the segment–segment potential  $U_{SS}$ , as defined by eq 3, is a function of six independent geometric parameters makes it also impossible to evaluate and tabulate the potential for all possible arrangements of interacting CNTs.

The number of independent geometric variables can be reduced if one or two of the limits of integration in eq 3 are set to infinity, defining the potentials for interaction between a finite segment and a semi-infinite nanotube ( $U_{Se}$ ) and between a segment and an infinitely long nanotube ( $U_{S\infty}$ ):

$$U_{Se}(h, \alpha, \xi_1, \xi_2, \eta_e) = \lim_{\eta_2 \rightarrow \infty} U_{SS}(h, \alpha, \xi_1, \xi_2, \eta_e, \eta_2) \quad (5)$$

$$U_{S\infty}(h, \alpha, \xi_1, \xi_2) = \lim_{\substack{\eta_1 \rightarrow -\infty \\ \eta_2 \rightarrow \infty}} U_{SS}(h, \alpha, \xi_1, \xi_2, \eta_1, \eta_2) \quad (6)$$

To make the notation more transparent, the location of the end of the semi-infinite nanotube in eq 5 and below is denoted as  $\eta_e$  rather than  $\eta_1$ . According to the rule that defines the direction of the  $\eta$ -axis (see above), eq 5 defines the potential

for a semi-infinite nanotube that extends from the point  $\eta_e$  in the positive direction of this axis.

The two potentials defined by eqs 5 and 6 cover the whole range of possible intertube interactions in systems consisting of multiple CNTs. In fact, due to the very large aspect ratio of CNTs, the vast majority of local intertube interactions in real CNT-based materials can be represented by eq 6. A relatively small fraction of the interactions that are affected by the ends of the CNTs requires the use of eq 5. The general segment–segment interaction potential given by eq 3 can also be expressed through the combination of two potentials for semi-infinite nanotubes:

$$U_{SS}(h, \alpha, \xi_1, \xi_2, \eta_1, \eta_2) = U_{Se}(h, \alpha, \xi_1, \xi_2, \eta_1) - U_{Se}(h, \alpha, \xi_1, \xi_2, \eta_2) \quad (7)$$

If both  $\eta_1$  and  $\eta_2$  are located on the same side of the  $\eta$ -axis from point  $O'$  (Figure 1a), the validity of the representation of  $U_{SS}$  in the form of eq 7 relies on the condition  $0 < \eta_1 < \eta_2$  that is the consequence of the rule defining the direction of  $\eta$ -axis. This condition ensures that the surfaces of the semi-infinite nanotubes originating at  $\eta_1$  or  $\eta_2$  and extending in the positive direction of the  $\eta$ -axis do not intersect with the surface of the  $(\xi_1, \xi_2)$  segment.

Despite the reduction of the number of independent variables to five in eq 5 and four in eq 6, the tabulation of  $U_{S\infty}(h, \alpha, \xi_1, \xi_2)$  and  $U_{Se}(h, \alpha, \xi_1, \xi_2, \eta_e)$  with sufficient accuracy is still impractical (or even impossible) due to limitations of computer memory. Therefore, the design of a computationally efficient intertube potential has to rely on approximate representations of  $U_{S\infty}$  and  $U_{Se}$ , that express them through one- and two-dimensional functions. Such functions can be evaluated and tabulated in advance, and used as needed in the course of a dynamic simulation. The formulation of an accurate and computationally efficient approximation of  $U_{S\infty}$  and  $U_{Se}$  is presented below, in sections 2.2 and 2.3.

**2.2. Potential  $U_{S\infty}$  for Interaction of a CNT Segment with an Infinitely Long CNT.** The potential for the interaction of a CNT segment with an infinitely long nanotube,  $U_{S\infty}(h, \alpha, \xi_1, \xi_2)$ , can be expressed as an integral of the density of the interaction potential,  $u_{\infty}(h, \alpha, \xi)$ , along the axis of the segment:

$$U_{S\infty}(h, \alpha, \xi_1, \xi_2) = \int_{\xi_1}^{\xi_2} u_{\infty}(h, \alpha, \xi) d\xi \quad (8)$$

The design of an approximate interaction potential, discussed below, is based on the introduction of an accurate approximation for the potential density  $\tilde{u}_{\infty}(h, \alpha, \xi)$ , which is then used in eq 8 to obtain the approximate interaction potential,  $\tilde{U}_{S\infty}(h, \alpha, \xi_1, \xi_2)$ .

In the case when the segment and the nanotube are parallel to each other ( $\sin \alpha = 0$ ), the potential density does not depend on  $\xi$  and eq 8 reduces to

$$U_{S\infty}(h, \xi_1, \xi_2) = (\xi_2 - \xi_1) u_{\infty}(h) \quad (9)$$

where

$$u_{\infty}(h) = n_{\sigma}^2 R_T^2 \int_0^{2\pi} \int_{-\infty}^{+\infty} \int_0^{2\pi} \varphi(r(h, \phi_1, \eta, \phi_2)) d\phi_2 d\eta d\phi_1 \quad (10)$$

is the potential density for parallel infinitely long nanotubes and  $r(h, \phi_1, \eta, \phi_2) = [(h + R_T(\cos \phi_2 - \cos \phi_1))^2 + R_T^2(\sin \phi_2 -$

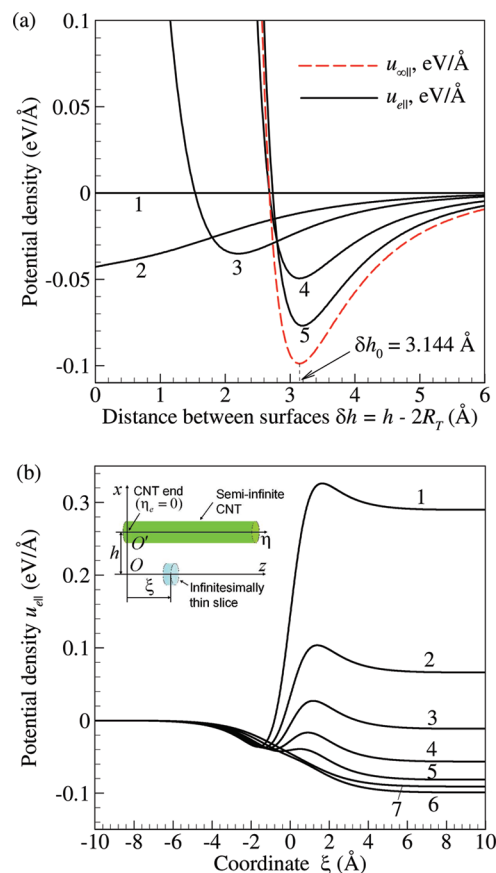


**Figure 2.** Potential densities for parallel infinitely long (dashed curve) and semi-infinite (solid curves) (10,10) single-walled CNTs,  $u_{\infty}(h)$  and  $u_{ell}(h, \xi)$ , shown as functions of the distance between the surfaces of the nanotubes,  $\delta h = h - 2R_T$  (a) and coordinate along the  $\xi$ -axis (b). In panel a, the potential densities for semi-infinite nanotubes,  $u_{ell}(h, \xi)$ , are shown for several values of  $\xi$  as marked by curves 1–5: (1)  $\xi = -r_c = -10.2$  Å, (2)  $\xi = -3$  Å, (3)  $\xi = -2$  Å, (4)  $\xi = 0$ , and (5)  $\xi = 2$  Å. The value of the equilibrium distance between the surfaces of infinitely long nanotubes,  $\delta h_0$ , is given in panel a. In panel b, the distributions of  $u_{ell}(h, \xi)$  are shown for several values of  $\delta h$  as marked by curves 1–7: (1)  $\delta h = 2.45$  Å, (2)  $\delta h = 2.60$  Å, (3)  $\delta h = 2.70$  Å, (4)  $\delta h = 2.80$ , (5)  $\delta h = 2.90$  Å, (6)  $\delta h = 3.15$  Å, and (7)  $\delta h = 3.40$  Å.

$\sin \phi_1)^2 + \eta^2]^{1/2}$ . The potential density for parallel nanotubes is a function of only one variable  $h$ . It can easily be calculated for a given interatomic potential  $\varphi(r)$ , recorded in a one-dimensional table with high accuracy, and used in mesoscopic simulations. The result of the direct numerical integration of eq 10 for (10,10) single-walled CNTs ( $R_T = 6.785$  Å) and interatomic potential given by eqs 1 and 2 is shown by the dashed curve in Figure 2a. The equilibrium distance between the surfaces of the CNTs,  $\delta h_0 = h_0 - 2R_T$  ( $h_0$  is the equilibrium distance between the axes of the CNTs), is found to be equal to 3.144 Å, close to the value  $\delta h_0 = 3.154$  Å obtained in ref 26 with slightly different parametrization of the interatomic Lennard-Jones potential.

The potential density for parallel nanotubes,  $u_{\infty}(h)$ , can be used in the design of an approximate representation of the potential density  $\tilde{u}_{\infty}(h, \alpha, \xi)$  for an arbitrary relative orientation of the segment and the nanotube. The idea of the approximation can be explained with the help of Figure 3, illustrating interaction between an infinitely long nanotube located on the  $\eta$ -axis and an infinitesimally thin slice of a nanotube segment located on the  $\xi$ -axis. The position of the slice on the axis is defined by coordinate  $\xi$ , the thickness of the slice is  $d\xi$ , and its

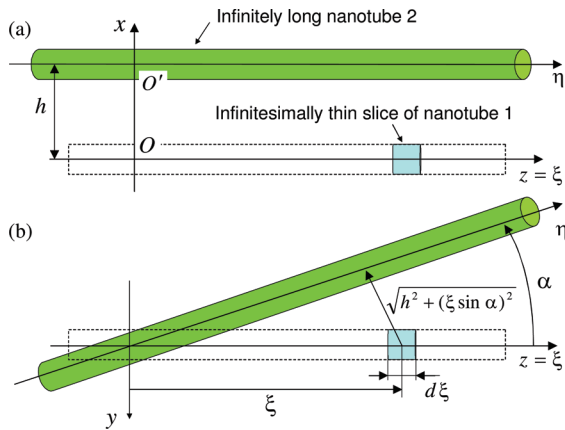


**Figure 3.** Schematic sketch illustrating the interaction between an infinitely long nanotube 2 located on the  $\eta$ -axis and an infinitesimally thin slice of a nanotube 1 located on the  $\xi$ -axis. The side and top views are shown in panels a and b, respectively. The distance from the center of the slice to the axis of nanotube 2 is equal to  $[h^2 + (\xi \sin \alpha)^2]^{1/2}$ .

surface area is  $dS = 2\pi R_T d\xi$ . The potential of the interaction between the surface of the slice and the infinitely long nanotube can be written as  $dU_{S\infty} = u_{\infty}(h, \alpha, \xi) d\xi$ . If we rotate the slice around its center so that the axis of the slice becomes parallel to the axis of the nanotube, then the new slice–tube potential density can be expressed through the potential density for parallel nanotubes:

$$\bar{u}_{\infty}(h, \alpha, \xi) = u_{\infty}(\sqrt{h^2 + (\xi \sin \alpha)^2}) \quad (11)$$

where  $[h^2 + (\xi \sin \alpha)^2]^{1/2}$  is the distance from the center of the slice to the axis of the nanotube. If angle  $\alpha$  is small, the rotation of the slice does not affect significantly the slice–tube interaction and the modified potential density given by eq 11 can be used to provide an approximation for the interaction potential,  $dU_{S\infty} \approx \bar{u}_{\infty}(h, \alpha, \xi) d\xi$ .

The quality of the approximation of the true potential density,  $u_{\infty}(h, \alpha, \xi)$ , by the potential density for the rotated slice,  $\bar{u}_{\infty}(h, \alpha, \xi)$ , can be assessed from Figure 4, where the distributions of the potential densities along the  $\xi$ -axis are shown for (10,10) single-walled CNTs. As expected, the quality of the approximation of  $u_{\infty}(h, \alpha, \xi)$  by  $\bar{u}_{\infty}(h, \alpha, \xi)$  is very good for small angles,  $\alpha \leq 10^\circ$ , and gradually deteriorates as  $\alpha$  approaches  $90^\circ$ .

The discrepancy between  $u_{\infty}(h, \alpha, \xi)$  and  $\bar{u}_{\infty}(h, \alpha, \xi)$  becomes smaller with a decrease in the nanotube radius and the ratio of these two functions approaches unity in the limit of infinitely thin nanotubes ( $R_T \rightarrow 0$ ). For nanotubes of finite radii, the quality of the approximation of the potential density at large angles can be improved by taking advantage of the fact that the distributions of  $\bar{u}_{\infty}(h, \alpha, \xi)$  are qualitatively similar to the distributions of  $u_{\infty}(h, \alpha, \xi)$  for any  $h$  and  $\alpha$ , Figure 4. This observation can be used to significantly improve the quantitative agreement between the true and approximate potential densities by introducing two scaling functions,  $\Gamma(h, \alpha)$  and  $\Omega(h, \alpha)$ , that scale the magnitude of function  $\bar{u}_{\infty}(h, \alpha, \xi)$  and its argument  $\xi$ , respectively. The new approximate potential density,  $\tilde{u}_{\infty}(h, \alpha, \xi)$ , can then be written in the following form:

$$\tilde{u}_{\infty}(h, \alpha, \xi) = \Gamma(h, \alpha) u_{\infty}(\sqrt{h^2 + (\xi \Omega(h, \alpha) \sin \alpha)^2}) \quad (12)$$

The choice of the scaling functions  $\Gamma(h, \alpha)$  and  $\Omega(h, \alpha)$  can be based on matching the locations of the minima of the true and approximate potential densities as well as their values at the minima. For any distance  $h$  and angle  $\alpha$  satisfying conditions  $2R_T < h < 2R_T + r_c$  and  $\sin \alpha \neq 0$ , each of the functions  $u_{\infty}(h, \alpha, \xi)$  and  $\bar{u}_{\infty}(h, \alpha, \xi)$  has either one minimum or two minima symmetrical with respect to  $\xi = 0$ . The presence of these minima is the direct consequence of the existence of the potential well in the interatomic potential  $\varphi(r)$ . In the case of the approximate potential density given by eq 11,  $\bar{u}_{\infty}(h, \alpha, \xi)$ , the transition from one minimum to two minima occurs precisely at  $\delta h = \delta h_0$  (one minimum for  $\delta h \geq \delta h_0$  and two minima for  $\delta h < \delta h_0$ ). For the true potential density,  $u_{\infty}(h, \alpha, \xi)$ , the transition is defined by both  $h$  and  $\alpha$ . For example, in Figure 4c, the distributions of  $u_{\infty}(h, \alpha, \xi)$  for  $\alpha = 10^\circ$  and  $\alpha = 30^\circ$  have only one minimum, while the distribution plotted for  $\alpha = 90^\circ$  has two minima (see inset in Figure 4c). We find, however, that for (10,10) single-walled CNTs all distributions have two minima at  $\delta h < \delta h_0 = 3.144$  Å and one minimum at  $\delta h \geq 3.159$  Å, regardless of  $\alpha$ . Thus, the dependence of the transition on  $\alpha$  is realized in a rather narrow range of  $\delta h$  and the transition criterion  $\delta h = \delta h_0$  can still be used for  $u_{\infty}(h, \alpha, \xi)$  as a rough approximation. The requirement to match the locations and values of the true and approximate potential densities at their minima is found to ensure a good agreement between the potential densities at arbitrary  $\xi$ . The scaling functions  $\Gamma(h, \alpha)$  and  $\Omega(h, \alpha)$  in eq 12 can then be determined from the minima-matching condition,  $\xi_{(\min)}(h, \alpha) = \bar{\xi}_{(\min)}(h, \alpha)$  and  $\tilde{u}_{\infty}(h, \alpha, \xi_{(\min)}(h, \alpha)) = u_{\infty}(h, \alpha, \bar{\xi}_{(\min)}(h, \alpha))$ , as follows:

$$\Gamma(h, \alpha) = \frac{u_{\infty}(h, \alpha, \xi_{(\min)}(h, \alpha))}{\bar{u}_{\infty}(h, \alpha, \bar{\xi}_{(\min)}(h, \alpha))}, \quad \Omega(h, \alpha) = \begin{cases} 1, & \bar{\xi}_{(\min)}(h, \alpha) = 0; \\ \frac{\xi_{(\min)}(h, \alpha)}{\bar{\xi}_{(\min)}(h, \alpha)}, & \bar{\xi}_{(\min)}(h, \alpha) < 0 \end{cases} \quad (13)$$

where  $\xi_{(\min)}(h, \alpha)$ ,  $\bar{\xi}_{(\min)}(h, \alpha)$ , and  $\bar{\xi}_{(\min)}(h, \alpha)$  are the locations of minima of functions  $u_{\infty}(h, \alpha, \xi)$ ,  $\bar{u}_{\infty}(h, \alpha, \xi)$ , and  $\tilde{u}_{\infty}(h, \alpha, \xi)$ , respectively. To simplify the notation, in the cases when two symmetrical minima are present, we consider the left minimum, so that  $\xi_{(\min)}$ ,  $\bar{\xi}_{(\min)}$ , and  $\bar{\xi}_{(\min)}$  are all negative.

Scaling functions  $\Gamma(h, \alpha)$  and  $\Omega(h, \alpha)$  can be calculated prior to simulations using the direct numerical evaluation of integrals defining  $u_{\infty}(h, \alpha, \xi)$  and  $u_{\infty}(h)$ , and then stored in two-dimensional tables. For any particular type of nanotubes, however, it is also possible to come up with analytical approximations of the scaling functions that would eliminate the necessity to use the two-dimensional tables. The analytical approximations should define non-negative periodic (with respect to angle  $\alpha$ ) functions that provide a good description of the numerical values given by eq 13 and satisfy the following conditions

$$\Gamma(h, \alpha) = \Omega(h, \alpha) = 1, \quad \frac{\partial \Gamma}{\partial \alpha}(h, \alpha) = \frac{\partial \Omega}{\partial \alpha}(h, \alpha) = 0 \quad \text{for} \quad \sin \alpha = 0 \quad (14)$$

These conditions ensure that the approximate potential density  $\tilde{u}_{\infty}(h, \alpha, \xi)$  and its derivative match the true density  $u_{|\infty}(h)$  and its derivative in the case when the segment and the nanotube are parallel to each other.

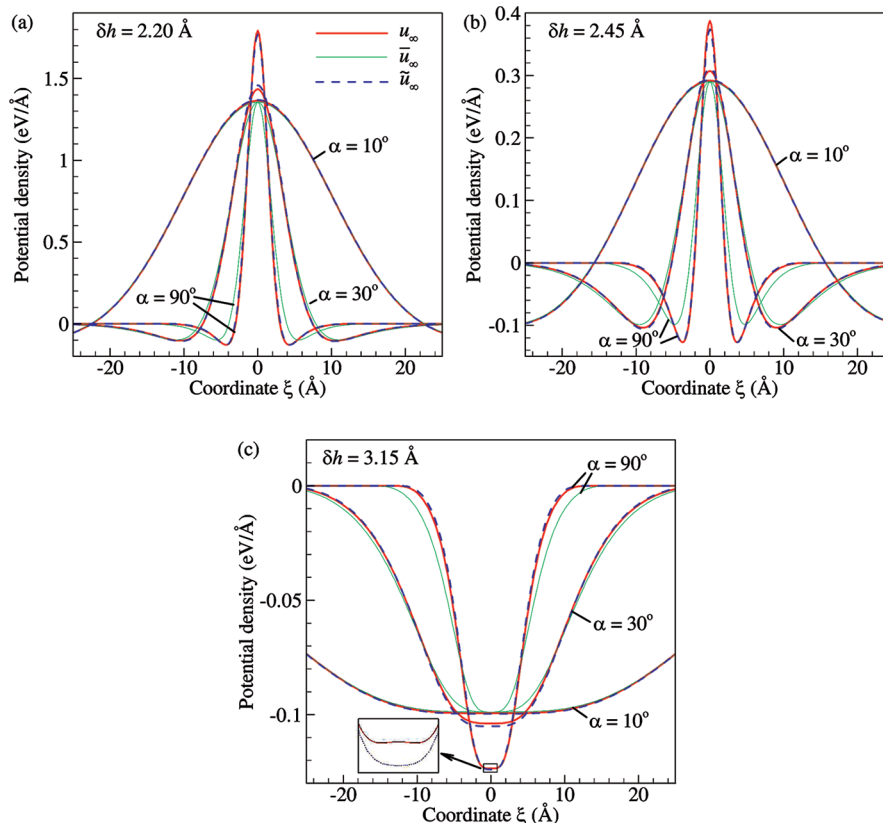


**Figure 4.** Distributions of true and approximate potential densities along the  $\xi$ -axes calculated for (10,10) single-walled CNTs ( $R_T = 6.785 \text{ \AA}$ ) for different values of  $h$  and  $\alpha$ . The true potential density,  $u_\infty(h, \alpha, \xi)$ , is shown by thick solid curves, the approximation given by eq 11,  $\tilde{u}_\infty(h, \alpha, \xi)$ , is shown by thin solid curves, and the approximation given by eq 18,  $\tilde{\tilde{u}}_\infty(h, \alpha, \xi)$ , is shown by dashed curves. The values of  $h$  correspond to the following distances between the surfaces of the nanotubes: (a)  $\delta h = h - 2R_T = 2.20 \text{ \AA}$ , (b)  $\delta h = 2.45 \text{ \AA}$ , and (c)  $\delta h = 3.15 \text{ \AA}$ . In most cases shown in the figure, the dashed curves visually coincide with the thick solid ones. The inset in panel c shows an enlarged view of the curves for  $\alpha = 90^\circ$  in the vicinity of  $\xi = 0$ . Two shallow minima at  $\xi = \pm 0.42 \text{ \AA}$  in the distribution of the true potential density  $u_\infty(h, \alpha, \xi)$  at  $\alpha = 90^\circ$  can be clearly identified in the inset. The distributions of  $u_\infty(h, \alpha, \xi)$  at  $\alpha = 10^\circ$  and  $\alpha = 30^\circ$  have a single minimum each at  $\xi = 0$ .

The search for analytical approximations for the scaling functions  $\Gamma(h, \alpha)$  and  $\Omega(h, \alpha)$  involves numerical calculation of the true potential density  $u_\infty(h_i, \alpha_j, \xi)$  for a large two-dimensional grid of points  $(h_i, \alpha_j)$ , identification of the positions of minima and calculation of the corresponding values of  $u_\infty(h_i, \alpha_j, \xi_{\min}(h_i, \alpha_j))$  for each point, and evaluation of the scaling functions  $\Omega_{i,j}$  and  $\Gamma_{i,j}$  directly from eq 13. Analytical or semianalytical approximations of functions  $\Gamma(h, \alpha)$  and  $\Omega(h, \alpha)$  can then be found by fitting to the values of  $\Omega_{i,j}$  and  $\Gamma_{i,j}$ .

Using the approach described above, a simple semianalytical form of the scaling functions has been found for single-walled CNTs with radii  $R_T$  ranging from 3.392 to 13.570  $\text{\AA}$ , which correspond to (5,5) and (20,20) nanotubes, respectively. This range covers the typical radii of single-walled CNTs produced by chemical vapor deposition,<sup>10</sup> high pressure carbon monoxide conversion (HiPco),<sup>40</sup> and laser ablation.<sup>2,40</sup> The scaling functions that provide a good fit to the numerical values obtained with eq 13 have the following form:

$$\Gamma(h, \alpha) = 1 + [\Gamma_\perp(h) - 1] \sin^2 \alpha \quad (15)$$

$$\Omega(\alpha) = \frac{1}{1 - C_\Omega \sin^2 \alpha} \quad (16)$$

where  $\Gamma_\perp(h) = \Gamma(h, \pi/2)$  is the scaling function for the nanotubes that are perpendicular to each other and  $C_\Omega$  is a constant. The dependence of  $\Omega(h, \alpha)$  on  $h$  is found to be weak and is neglected

in eq 16. The functions defined by eqs 15 and 16 satisfy the conditions given by eq 14. Formally, eqs 15 and 16 can be considered as three-term Taylor series expansions of even functions  $\Gamma(h, \alpha)$  and  $\Omega^{-1}(\alpha)$  into power series of  $\sin \alpha$ . However, as shown below, in contrast to the expectation for the Taylor expansion, these relationships provide good approximations of the functions defined by eq 13 not only for small  $\sin \alpha$  but for any angles between the interacting nanotubes.

The scaling function for perpendicular nanotubes,  $\Gamma_\perp(h)$ , is determined in a two-step fitting procedure. First, a table of values of  $\Gamma_\perp(h)$  is calculated for a given  $R_T$  using eq 13, i.e.,  $\Gamma_\perp(h) = u_\infty(h, \pi/2, \xi_{\min}(h, \pi/2)) / \tilde{u}_\infty(h, \pi/2, \xi_{\min}(h, \pi/2))$ , where  $u_\infty(h, \pi/2, \xi_{\min}(h, \pi/2))$  is found by direct numerical integration. Second, the cubic spline interpolation<sup>47</sup> is used to obtain a continuously differentiable function passing through each of the values in the table. The values of  $\Gamma_\perp(h)$  used in the interpolation along with the corresponding spline curves are shown in Figure 5 for (5,5), (10,10), and (20,20) single-walled CNTs. One can see that values of  $\Gamma_\perp(h)$  increase with increasing  $R_T$  (formally,  $\Gamma_\perp(h) \rightarrow 1$  when  $R_T \rightarrow 0$ ), and the slopes of the curves change in an abrupt manner at distances around the equilibrium intertube separation, i.e., at  $\delta h \approx \delta h_0$ . The shape of  $\Gamma_\perp(h)$  is relatively simple and can be further approximated by an analytic relationship; e.g., as a rough approximation,  $\Gamma_\perp(h)$  can be represented by two lines intersecting at  $\delta h \approx \delta h_0$ . All calculations reported in this paper, however, are performed with the spline approximation of  $\Gamma_\perp(h)$  shown in Figure 5.

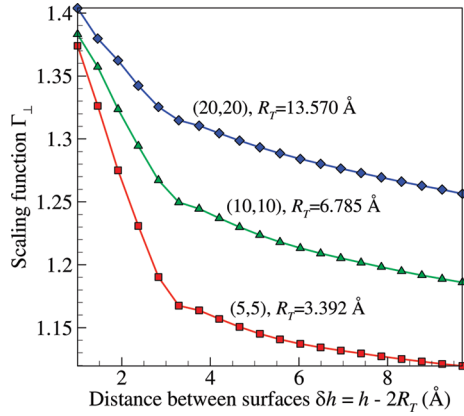


**Figure 5.** Scaling function for nanotubes perpendicular to each other,  $\Gamma_{\perp}(h)$ , as a function of the distance between the surfaces of nanotubes,  $\delta h = h - 2R_T$ . The values shown by symbols are calculated using eq 13 with  $\alpha = \pi/2$  for (5,5), (10,10), and (20,20) single-walled CNTs. The curves show the result of cubic spline interpolation between the calculated points.

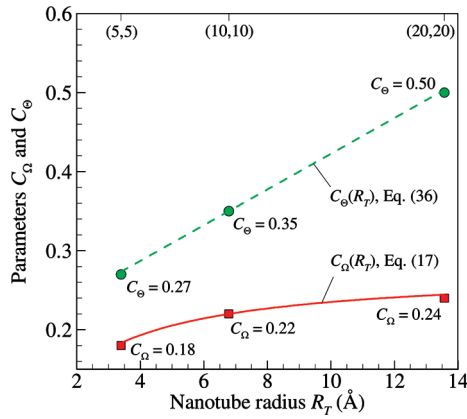


**Figure 6.** Parameters  $C_{\Omega}$  and  $C_{\Theta}$  of scaling functions given by eqs 16 and 35, respectively. The parameters are calculated for (5,5), (10,10), and (20,20) single-walled CNTs, with values shown in the figure. The solid and dashed curves show approximations of the dependences of the parameters on the nanotube radius given by eqs 17 and 36, respectively.

The values of the constant  $C_{\Omega}$  in eq 16 can be found for various  $R_T$  numerically, e.g., using the square-root method to find the best agreement between  $\Omega_{ij}$  calculated with eq 13 and the values predicted by eq 16. The result of the calculation of  $C_{\Omega}$  for (5,5), (10,10), and (20,20) single-walled CNTs is shown in Figure 6 by square symbols. The value of  $C_{\Omega}$  exhibits a weak increase with  $R_T$  which, within the range of radii considered in this work, can be well described by a simple analytical function,

$$C_{\Omega}(R_T) = 0.275 \left( 1 - \frac{1}{1 + 0.59R_T} \right) \quad (17)$$

This function is plotted in Figure 6 by the solid curve. The approximation given by eq 17 satisfies the condition that requires  $C_{\Omega}$  to vanish when  $R_T$  approaches zero, suggesting that eq 17 is likely to be appropriate for nanotubes with radii smaller than the radius of the (5,5) single-walled CNT.

Using the approximations of the scaling functions given by eqs 15 and 16, the final form of the approximate potential density can be written as follows:

$$\tilde{u}_{\infty}(h, \alpha, \xi) = \Gamma(h, \alpha) u_{\text{opt}}(\sqrt{h^2 + (\xi\Omega(\alpha) \sin \alpha)^2}) \quad (18)$$

The distributions of the approximate potential density  $\tilde{u}_{\infty}(h, \alpha, \xi)$ , calculated for (10,10) single-walled CNTs with fitting functions given by eqs 15 and 16, are shown in Figure 4 by dashed curves. The quantitative agreement between this simple approximation and the true potential density is surprisingly good, so that  $\tilde{u}_{\infty}(h, \alpha, \xi)$  can be used for the analysis of properties of the true potential density  $u_{\infty}(h, \alpha, \xi)$ . In particular, the positions of the minima of  $u_{\infty}(h, \alpha, \xi)$  can be estimated from eq 18 as follows:  $\xi_{\min}(h, \alpha) \approx \pm(h_0^2 - h^2)^{1/2}/(\Omega(\alpha) \sin \alpha)$  for  $h < h_0$  and  $\xi_{\min}(h, \alpha) = 0$  for  $h \geq h_0$ .

The design of the approximation of the potential density given by eq 18 (or its generalization in the form of eq 12) is the key result of this paper. With the help of two tabulated one-dimensional functions,  $u_{\text{opt}}(h)$  and  $\Gamma_{\perp}(h)$ , this equation allows for a straightforward and computationally efficient calculation of the potential density for an arbitrary relative orientation of an infinitely long nanotube and a segment.

By inserting the approximation for the potential density  $\tilde{u}_{\infty}(h, \alpha, \xi)$  into eq 8, one can obtain an approximate potential describing the interaction of a CNT segment with an infinitely long nanotube. For the case of nonparallel CNTs ( $\sin \alpha \neq 0$ ), the approximate interaction potential can be written as

$$\tilde{U}_{\text{Soo}}(h, \alpha, \xi_1, \xi_2) = \int_{\xi_1}^{\xi_2} \tilde{u}_{\infty}(h, \alpha, \xi) d\xi = \Gamma(h, \alpha) \int_{\xi_1}^{\xi_2} u_{\text{opt}}(\sqrt{h^2 + (\xi\Omega(h, \alpha) \sin \alpha)^2}) d\xi \quad (19)$$

Introducing a new variable  $\bar{\xi} = \xi\Omega(\alpha) \sin \alpha$ , one can rewrite eq 19 in the following form:

$$\tilde{U}_{\text{Soo}}(h, \alpha, \xi_1, \xi_2) = \frac{\Gamma(h, \alpha)}{\Omega(\alpha) \sin \alpha} I(h, \xi_1 \Omega(\alpha) \sin \alpha, \xi_2 \Omega(\alpha) \sin \alpha) \quad (20)$$

$$I(h, \xi_1, \xi_2) = \int_{\xi_1}^{\xi_2} u_{\text{opt}}(\sqrt{h^2 + \bar{\xi}^2}) d\bar{\xi} \quad (21)$$

The function given by eq 21 can be split into two two-dimensional functions:

$$I(h, \xi_1, \xi_2) = \Phi(h, \xi_2) - \Phi(h, \xi_1) \quad (22)$$

$$\Phi(h, \xi) = \int_{\text{sgn}(\xi)\xi_{\min}(h)}^{\xi} u_{\text{opt}}(\sqrt{h^2 + \bar{\xi}^2}) d\bar{\xi} = \text{sgn}(\xi) \int_{\xi_{\min}(h)}^{|\xi|} u_{\text{opt}}(\sqrt{h^2 + \bar{\xi}^2}) d\bar{\xi} \quad (23)$$

where  $\text{sgn}(\xi)$  is the sign function and the lower limit of the integral in eq 23 is introduced to ensure that function  $u_{\text{opt}}$  is defined in the whole range of the integration. The potential density  $u_{\text{opt}}$  is not defined for arguments that are smaller than  $2R_T$ , when the surfaces of the interacting nanotubes intersect each other. The argument of  $u_{\text{opt}}$  in eq 23 is always larger than  $2R_T$  if  $h > 2R_T$ . In this case, the integral in eq 23 is defined for any possible values of  $\alpha$ ,  $\xi_1$ , and  $\xi_2$ , and  $\xi_{\min}(h) = 0$  can be used.

In the case when  $h < 2R_T$ , however, the existence of the integral in eq 23 can only be ensured by a proper choice of  $\zeta_{\min}(h) > 0$ . With the convention used to define the directions of the axes in Figure 1a, the case  $h < 2R_T$  may occur only if  $\xi_2 \geq \xi_1 > 0$ . Therefore, the values of arguments  $\zeta_1$  and  $\zeta_2$  of function  $I(h, \zeta_1, \zeta_2)$  in eq 20 have the same sign, so that the integration interval in eq 21 does not include the point  $\zeta = 0$ . This enables introduction of a continuously differentiable function  $\zeta_{\min}(h)$  that satisfies, for any given  $h$ , the condition  $[h^2 + \zeta_{\min}^2(h)]^{1/2} > 2R_T$ . To enable the design of function  $\zeta_{\min}(h)$  and to ensure that this function does not exceed the minimum possible values of  $|\zeta|$  in eq 23, a small positive constant  $\Delta$  is introduced to limit the function  $\zeta_{\min}(h)$  from above,  $[h^2 + \zeta_{\min}^2(h)]^{1/2} < 2R_T + \Delta$ . Physically, the latter condition implies that configurations where surfaces of the segment and the nanotube are very close to each other (and have a very high interaction energy) are not considered. Taken together, the requirements for the design of the function  $\zeta_{\min}(h)$  can be formulated as follows:

$$\begin{aligned} 2R_T < \sqrt{h^2 + \zeta_{\min}^2(h)} < 2R_T + \Delta, & \text{ if } h < 2R_T + \Delta; \\ \zeta_{\min}(h) = 0, & \text{ if } h \geq 2R_T + \Delta \end{aligned} \quad (24)$$

The function  $\zeta_{\min}(h)$  is not unique and can be chosen in various ways. An example of function  $\zeta_{\min}(h)$  that satisfies the above conditions is given in section S1 of the Supporting Information.

The final computationally efficient expression of the approximate interaction potential can be obtained by inserting eq 22 into the right part of eq 20:

$$\tilde{U}_{S_{\infty}}(h, \alpha, \xi_1, \xi_2) = \frac{\Gamma(h, \alpha)}{\Omega(\alpha) \sin \alpha} [\Phi(h, \xi_2 \Omega(\alpha) \sin \alpha) - \Phi(h, \xi_1 \Omega(\alpha) \sin \alpha)] \quad (25)$$

The approximate interaction potential given by eq 25 is expressed through two-dimensional functions  $\Gamma(h, \alpha)$  and  $\Phi(h, \zeta)$  and one-dimensional function  $\Omega(\alpha)$ . The function  $\Phi(h, \zeta)$  can be calculated for an arbitrary  $h$  and  $\zeta$  by numerical integration of eq 23, whereas the scaling functions  $\Gamma(h, \alpha)$  and  $\Omega(\alpha)$  can be evaluated using semianalytical expressions designed for a particular type of nanotubes, e.g., eqs 15 and 16. The values of these functions can be recorded in one- and two-dimensional tables, enabling even more efficient evaluation of the interaction potential in a dynamic simulation of a large number of interacting CNTs (e.g., section 4) by an interpolation of the tabulated values. Some practical considerations related to the numerical implementation of the interaction potential defined by eq 25 are discussed in section S1 of the Supporting Information.

The range of applicability of eq 25 does not include the case of parallel nanotubes, as the right part of this equation has an indeterminate form for  $\sin \alpha \neq 0$ . By applying l'Hôpital's rule and taking into account conditions given by eq 14, however, one can prove that

$$\lim_{\sin \alpha \rightarrow 0} \tilde{U}_{S_{\infty}}(h, \alpha, \xi_1, \xi_2) = U_{S_{\infty}}(h, \xi_1, \xi_2) \quad (26)$$

This means that eq 25 approaches correct values given by eq 9 in the limit of parallel nanotubes.

The quality of the approximation given by eq 25 with scaling functions taken in the form of eqs 15 and 16 can be assessed from Figure 7, where the true potential  $U_{S_{\infty}}(h, \alpha, \xi_1, \xi_2)$  evaluated through the direct integration of eq 3 is compared with the approximate potential  $\tilde{U}_{S_{\infty}}(h, \alpha, \xi_1, \xi_2)$ . The interaction potentials are plotted as functions of angle  $\alpha$  for fixed coordinates of the nanotube segment ( $\xi_1 = -10 \text{ \AA}$ ,  $\xi_2 = 10 \text{ \AA}$ ) and several values of intertube distance  $h$  and nanotube radius  $R_T$ . The dependence of the true potential on  $\alpha$  is sensitive to the intertube distance and can be quite complex. In particular, as the distance  $h$  changes, the angle  $\alpha$  that corresponds to local minima of energy spans the range from parallel to perpendicular orientations of the segment and the nanotube. All of the peculiarities of the angular dependences of the true potential, however, are well reproduced by the approximate potential. Although the discrepancy between the approximate and true potentials  $|\tilde{U}_{S_{\infty}} - U_{S_{\infty}}|$  tends to increase with increasing radius of the nanotubes, the approximation remains fairly accurate in the range of  $R_T$  considered in the parametrization; e.g.,  $|\tilde{U}_{S_{\infty}} - U_{S_{\infty}}|$  is less than 5% for the data shown in Figure 7. The discrepancy can be further reduced by fine-tuning of the parametrization for a particular type of nanotubes or by a more elaborate design of scaling functions. For example, an alternative set of more complicated scaling functions introduced in ref 48 is found to provide a slightly better accuracy of the representation of the true potential. Nevertheless, the accuracy achieved with simple scaling functions given by eqs 15 and 16 is likely to be sufficient for the majority of applications of the potential, e.g., for computational analysis of the dynamic behavior of large ensembles of nanotubes illustrated in section 4.

**2.3. Potential  $U_{S_e}$  for Interaction of a CNT Segment with a Semi-Infinite CNT.** The approximate interaction potential for a nanotube segment and an infinitely long CNT, discussed in the previous section, is capable of describing intertube interactions that do not involve ends of the nanotubes. To complete the interaction model and to account for any possible spatial arrangement of finite-length CNTs, a computationally efficient approximation of the potential describing the interaction between a nanotube segment and a semi-infinite nanotube, eq 5, is considered next. The logic and basic steps used in the design of the approximate potential for a semi-infinite nanotube,  $\tilde{U}_{S_e}(h, \alpha, \xi_1, \xi_2, \eta_e)$ , are similar to the ones used in the previous section for the case of an infinitely long nanotube.

Similar to eq 8 for  $U_{S_{\infty}}(h, \alpha, \xi_1, \xi_2)$ ,  $U_{S_e}(h, \alpha, \xi_1, \xi_2, \eta_e)$  can be represented in the form of an integral of the potential density along the axis of the segment

$$U_{S_e}(h, \alpha, \xi_1, \xi_2, \eta_e) = \int_{\xi_1}^{\xi_2} u_e(h, \alpha, \xi, \eta_e) d\xi \quad (27)$$

where  $u_e(h, \alpha, \xi, \eta_e)$  is the potential density created due to the interaction with a semi-infinite nanotube.

In the case of parallel nanotubes, it is convenient to place the origin of the Cartesian coordinates so that the axis  $Ox$  goes through the end of the semi-infinite nanotube (Figure 1b). This eliminates the dependence of the potential density on  $\eta_e$  and reduces eq 27 to

$$U_{S_{\text{ell}}}(h, \xi_1, \xi_2) = \int_{\xi_1}^{\xi_2} u_{\text{ell}}(h, \xi) d\xi \quad (28)$$

where

$$u_{\text{el}}(h, \xi) = n_{\sigma}^2 R_T^2 \int_0^{2\pi} \int_0^{+\infty} \int_0^{2\pi} \varphi(r(h, \xi, \phi_1, \eta, \phi_2)) d\phi_2 d\eta d\phi_1 \quad (29)$$

is the potential density created in a nanotube oriented along the  $\xi$ -axis by a parallel semi-infinite nanotube oriented along the  $\eta$ -axis. The distance between points on the surfaces of the nanotubes can be calculated in this case as  $r(h, \xi, \phi_1, \eta, \phi_2) = [(h + R_T(\cos \phi_2 - \cos \phi_1))^2 + R_T^2(\sin \phi_2 - \sin \phi_1)^2 + (\eta - \xi)^2]^{1/2}$ .

To illustrate the dependence of the potential density  $u_{\text{el}}(h, \xi)$  on the geometric parameters, the results of numerical integration of eq 29 for (10,10) single-walled CNTs are shown in Figure 2 for several fixed values of  $h$  and  $\xi$ . At negative  $\xi$  (curves 1–3 in Figure 2a), the density  $u_{\text{el}}(h, \xi)$  exists for any  $h \geq 0$ , which is different from  $u_{\text{sol}}(h)$  that is defined only for  $h \geq 2R_T$ . At  $\xi < -r_c$ , the value of  $u_{\text{el}}(h, \xi)$  is zero for any  $h$ , whereas, at  $\xi \geq r_c$ , the density distribution  $u_{\text{el}}(h, \xi)$  is independent of  $\xi$  and coincides with the one shown in Figure 2a for  $u_{\text{sol}}(h)$ . The distributions of  $u_{\text{el}}(h, \xi)$  along  $\xi$  (Figure 2b) are monotonous for  $\delta h > 2.94 \text{ \AA}$ , when the attraction dominates the interaction between the CNT slice and the semi-infinite CNT. For  $\delta h < 2.94 \text{ \AA}$ , on the other hand, the distribution attains a more complex shape, with a minimum and a maximum appearing due to the changes in the relative contributions of the attractive and repulsive interactions as the position of the slice  $\xi$  passes in the proximity of the nanotube end. The threshold value of  $\delta h = 2.94 \text{ \AA}$  for the appearance of extrema on the distributions shown in Figure 2b corresponds to the separation that yields zero interaction energy for two slices located in the same plane (i.e., slices of parallel nanotubes at  $\xi = \eta$ ).

Similar to eq 11, for small angles  $\alpha$  ( $\alpha \leq 10^\circ$ ), the potential density  $u_e(h, \alpha, \xi, \eta_e)$  can be approximated by considering slices of the nanotube segment rotated to orient them parallel to the semi-infinite nanotube (see section 2.2 for a detailed discussion):

$$\bar{u}_e(h, \alpha, \xi, \eta_e) = u_{\text{el}}(\sqrt{h^2 + (\xi \sin \alpha)^2}, \xi \cos \alpha - \eta_e) \quad (30)$$

where  $[h^2 + (\xi \sin \alpha)^2]^{1/2}$  is the distance from the center of the slice to the axis of the semi-infinite nanotube and  $\xi \cos \alpha - \eta_e$  is the distance between the nanotube end and the projection of the center of the slice on the axis of the nanotube (Figure 8). The quality of the approximation of the true potential density  $u_e(h, \alpha, \xi, \eta_e)$  by the potential density of the rotated slices  $\bar{u}_e(h, \alpha, \xi, \eta_e)$  deteriorates as angle  $\alpha$  increases. Nevertheless, similar to the potential density for an infinitely long nanotube, an introduction of scaling function can ensure that the difference between the approximate and true potential densities remains small at any angles. Out of a variety of ways the scaling functions can be introduced, below we consider an approach that makes use of the scaling functions already introduced in section 2.2. With the use of scaling functions  $\Gamma(h, \alpha)$  and  $\Omega(\alpha)$  defined by eqs 15 and 16, the next approximation of the potential density can be written as

$$\bar{u}_e^*(h, \alpha, \xi, \eta_e) = \Gamma(h, \alpha) u_{\text{el}}(\sqrt{h^2 + (\xi \Omega(\alpha) \sin \alpha)^2}, \xi \cos \alpha - \eta_e) \quad (31)$$

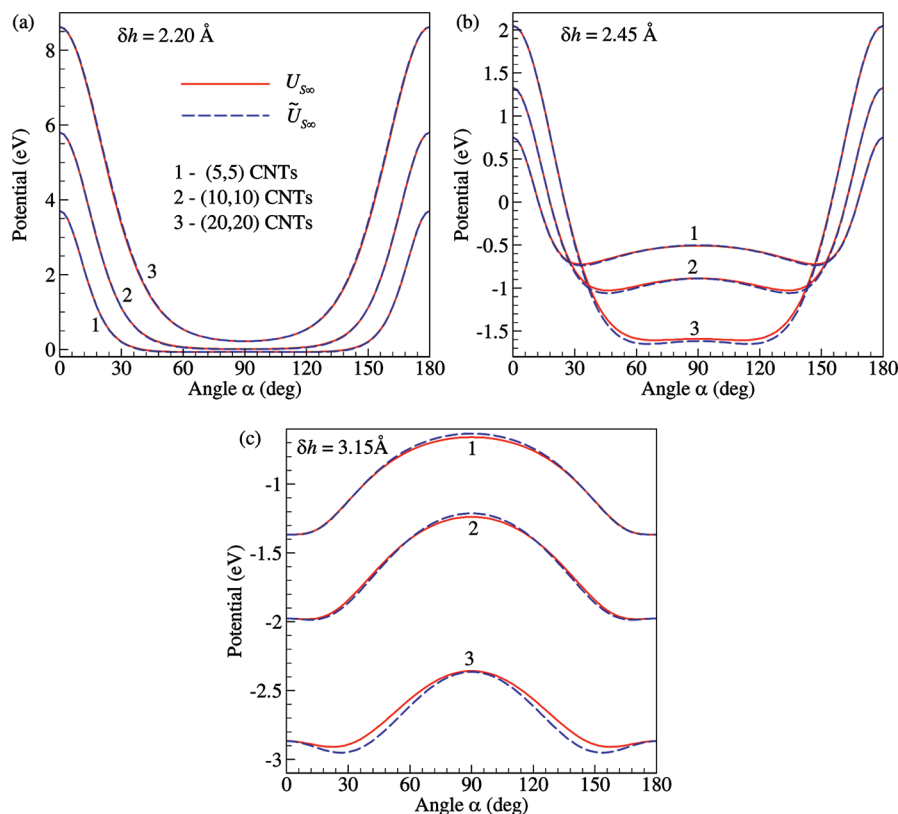


**Figure 7.** True and approximate potentials for interaction between an infinitely long single-walled CNT with a nanotube segment. The true potential  $U_{\text{sol}}(h, \alpha, \xi_1, \xi_2)$  (solid curves, eqs 3 and 6) and the approximate potential  $\tilde{U}_{\text{sol}}(h, \alpha, \xi_1, \xi_2)$  (dashed curves, eq 25) are shown as functions of angle  $\alpha$  for constant coordinates of the segment ends ( $\xi_1 = -10 \text{ \AA}$ ,  $\xi_2 = 10 \text{ \AA}$ ) and three distances between the surfaces of the nanotubes: (a)  $\delta h = h - 2R_T = 2.20 \text{ \AA}$ , (b)  $\delta h = 2.45 \text{ \AA}$ , and (c)  $\delta h = 3.15 \text{ \AA}$ . Curves 1–3 are shown for (5,5), (10,10), and (20,20) single-walled CNTs, respectively. In panel a, the solid and dashed curves visually coincide with each other.

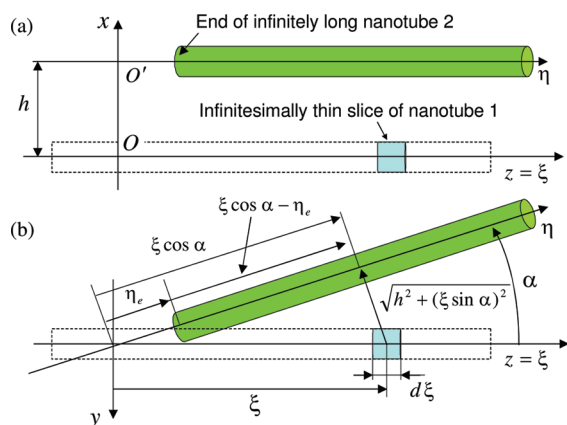


**Figure 8.** Schematic sketch illustrating the interaction between a semi-infinite nanotube 2 located on the  $\eta$ -axis and an infinitesimally thin slice of a nanotube 1 located on the  $\xi$ -axis. The side and top views are shown in panels a and b, respectively. The location of the center of the slice with respect to nanotube 2 can be characterized by distances  $[h^2 + (\xi \sin \alpha)^2]^{1/2}$  and  $\xi \cos \alpha - \eta_e$ .

The quality of this approximation can be assessed from Figure 9, where the true,  $u_e(h, \alpha, \xi, \eta_e)$ , and approximate,  $\bar{u}_e^*(h, \alpha, \xi, \eta_e)$ , potential densities are plotted for (10,10) single-walled CNTs by thick and thin solid curves, respectively. The distributions of the potential density created by the interaction with a semi-infinite nanotube are more complicated as compared to the case of an infinitely long nanotube (Figure 4). In particular, the distributions of  $u_e(h, \alpha, \xi, \eta_e)$  along the  $\xi$ -axis are no longer symmetric with respect to the center of coordinates ( $\xi = 0$ ) for any angle except for the case of perpendicular nanotubes. Moreover, a variation of  $h$ ,  $\alpha$ , or  $\eta_e$  results in qualitative changes in the shapes of the curves. Despite the complexity of the dependence of the potential density on the geometric parameters, the approximation given by eq 31 provides a fairly accurate description of the true density.

The quality of the approximation can be further improved by introducing an additional scaling function into eq 31. Similar to the design of scaling functions  $\Gamma(h, \alpha)$  and  $\Omega(\alpha)$  described in section 2.2, the additional scaling function can be chosen on the basis of a condition requiring matching the values of the true and approximate potential densities in their minima. It is possible to use this condition, since distributions of  $\bar{u}_e^*(h, \alpha, \xi, \eta_e)$  and  $u_e(h, \alpha, \xi, \eta_e)$  along  $\xi$  at  $\sin \alpha \neq 0$  have at least one local minimum (e.g., see Figure 9), where they take values  $\bar{u}_{(\min)}^*(h, \alpha, \eta_e)$  and  $u_{(\min)}(h, \alpha, \eta_e)$ , respectively. In the case when functions have several local minima, we apply the minima-matching condition to the minimum corresponding to smallest  $\xi$ . The scaling function is applied to coordinate  $\eta_e$ , so that the scaled coordinate  $\bar{\eta}_e = \bar{\eta}_e(h, \alpha, \eta_e)$  is found from the following condition:  $\bar{u}_{(\min)}^*(h, \alpha, \bar{\eta}_e) = u_{(\min)}(h, \alpha, \eta_e)$ . The approximate potential density can then be reformulated as follows:

$$\bar{u}_e(h, \alpha, \xi, \eta_e) = \Gamma(h, \alpha) u_{\text{cil}} \left( \sqrt{h^2 + (\xi \Omega(\alpha) \sin \alpha)^2}, \xi \cos \alpha - \Theta(h, \alpha, \eta_e) \eta_e \right) \quad (32)$$

where the new scaling function  $\Theta(h, \alpha, \eta_e)$  is defined as

$$\Theta(h, \alpha, \eta_e) = \begin{cases} 1, & \eta_e = 0; \\ \frac{\bar{\eta}_e(h, \alpha, \eta_e)}{\eta_e}, & \eta_e \neq 0 \end{cases} \quad (33)$$

Similar to functions  $\Gamma(h, \alpha)$  and  $\Omega(h, \alpha)$ , it is not necessary to calculate the values of  $\Theta(h, \alpha, \eta_e)$  by direct evaluation of eq 33. Instead,  $\Theta(h, \alpha, \eta_e)$  can be approximated by a positive, bounded, and periodic (with respect to angle  $\alpha$ ) function satisfying the following conditions:

$$\Theta(h, \alpha, \eta_e) = 1 \quad \text{and} \quad \frac{\partial \Theta}{\partial \alpha}(h, \alpha, \eta_e) = 0 \quad \text{for} \quad \sin \alpha = 0 \quad (34)$$

The conditions given by eq 34 ensure that, in the case when the nanotube segment and the semi-infinite nanotube are parallel to each other, eq 32 reduces to the one for the potential density for parallel nanotubes,  $\bar{u}_e(h, \alpha, \xi, \eta_e) = u_{\text{cil}}(h, \xi - \eta_e)$ , whereas forces and torques calculated with the approximate potential density are equal to the ones calculated with the true potential density. The condition that  $\Theta(h, \alpha, \eta_e)$  is a positive bounded function ensures that

$$\lim_{\eta_e \rightarrow +\infty} \bar{u}_e(h, \alpha, \xi, \eta_e) = 0 \quad \text{and} \quad \lim_{\eta_e \rightarrow -\infty} \bar{u}_e(h, \alpha, \xi, \eta_e) = \bar{u}_{\infty}(h, \alpha, \xi)$$

An analytical approximation of the scaling function  $\Theta(h, \alpha, \eta_e)$  for single-walled CNTs of a given radius  $R_T$  is obtained as follows. The true potential density  $u_e(h, \alpha, \xi, \eta_e)$  is first calculated as a function of  $\xi$  for a large three-dimensional grid of parameters ( $h, \alpha, \eta_e$ ) by direct numerical integration. The values of the scaling function,  $\Theta_{i,j,k} = \Theta(h_i, \alpha_j, \eta_{ek})$ , are then determined at each point of the grid by matching the minima of the true and approximate potential density functions, eq 33. Analysis of the results of the calculations performed for single-walled CNTs with radii ranging from 3.392 to 13.570 Å suggests that the dependence of  $\Theta(h, \alpha, \eta_e)$  on  $h$  and  $\eta_e$  is relatively weak and can be neglected. Moreover, the following simple function is found to provide a good description of the numerical values and satisfaction of the conditions given by eq 34:

$$\Theta(h, \alpha, \eta_e) = \Theta(\alpha) = 1 - C_{\Theta} \sin^2 \alpha \quad (35)$$

where  $C_{\Theta}$  is a constant for a given radius of nanotubes. The values of  $C_{\Theta}$  can be found for different  $R_T$  numerically, e.g., using the square-root method to find the best agreement between the values  $\Theta_{i,j,k}$  determined as described above and the corresponding values given by eq 35. For the nanotubes considered in this work ( $R_T$  ranges from 3.392 to 13.570 Å), the values of  $C_{\Theta}$  (shown by circular symbols in Figure 6) can be approximated by a linear dependence on  $R_T$ :

$$C_{\Theta}(R_T) = 0.35 + 0.0226(R_T - 6.785) \quad (36)$$

This linear dependence is shown in Figure 6 by a dashed line. In contrast to eq 17, this approximation of  $C_{\Theta}(R_T)$  does not satisfy the condition of  $\lim_{R_T \rightarrow 0} C_{\Theta}(R_T) = 0$  which is required to ensure the agreement between the true and approximate potential densities in the limit of infinitely thin nanotubes. Therefore, the applicability of eq 36 for nanotubes with radii smaller than the radius of the (5,5) CNT is questionable.

Using the approximation of the scaling function given by eq 35, the final form of the approximate potential density can be written as follows:

$$\tilde{u}_e(h, \alpha, \xi, \eta_e) =$$

$$\Gamma(h, \alpha) u_{\text{ell}}(\sqrt{h^2 + (\xi \Omega(\alpha) \sin \alpha)^2}, \xi \cos \alpha - \Theta(\alpha) \eta_e) \quad (37)$$

The distributions of the approximate potential density  $\tilde{u}_e(h, \alpha, \xi, \eta_e)$ , predicted with eq 37 for (10,10) single-walled CNTs, are shown in Figure 9 by dashed curves. A comparison of these approximate distributions with the true potential density distributions demonstrates a substantial improvement in the quality of approximation achieved by the introduction of the additional scaling function  $\Theta(\alpha)$ . The improvement is particularly notable for  $\eta_e > 0$ , where the approximation given by eq 31 shows substantial deviations from the true potential density.

The approximation for the potential density given by eq 37 can be used in eq 27, resulting in the following formulation of

an approximate potential describing the interaction of a CNT segment with a semi-infinite nanotube:

$$\begin{aligned} \tilde{U}_{\text{Se}}^*(h, \alpha, \xi_1, \xi_2, \eta_e) &= \int_{\xi_1}^{\xi_2} \tilde{u}_e(h, \alpha, \xi, \eta_e) d\xi = \\ \Gamma(h, \alpha) \int_{\xi_1}^{\xi_2} u_{\text{ell}}(\sqrt{h^2 + (\xi \Omega(\alpha) \sin \alpha)^2}, \xi \cos \alpha - \Theta(\alpha) \eta_e) d\xi \end{aligned} \quad (38)$$

The integral in eq 38 cannot be easily expressed through one- and two-dimensional functions of the geometric parameters and has to be calculated by numerical integration of the potential density along the segment axis. In this work, we use the following simple method of numerical integration. The segment

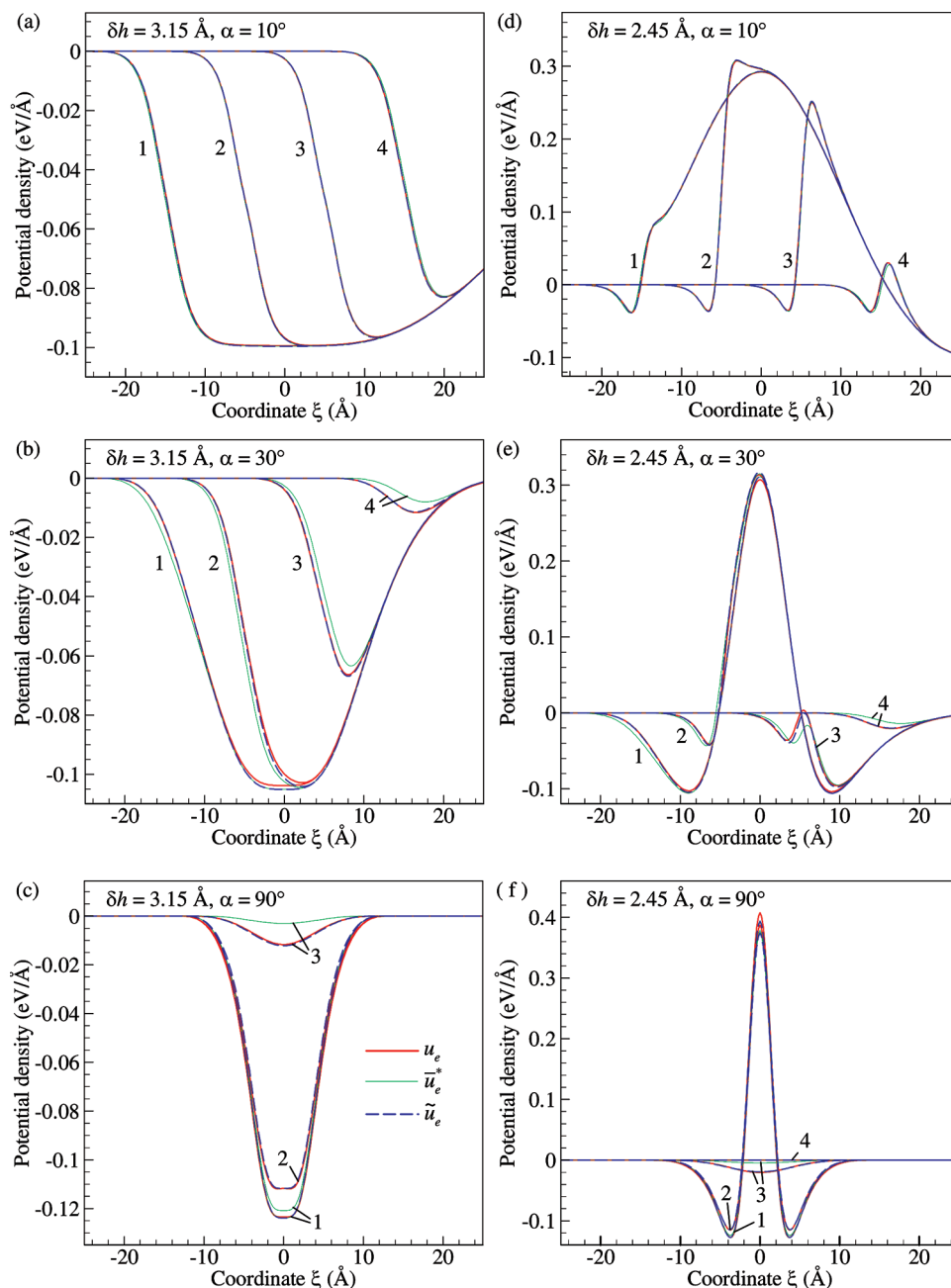


**Figure 9.** Distributions of true and approximate potential densities along the  $\xi$ -axes calculated for (10,10) single-walled CNTs ( $R_T = 6.785 \text{ \AA}$ ) for different values of  $h$ ,  $\alpha$ , and  $\eta_e$ . The true potential density,  $u_e(h, \alpha, \xi, \eta_e)$ , is shown by thick solid curves, the approximation given by eq 31,  $\tilde{u}_e^*(h, \alpha, \xi, \eta_e)$ , is shown by thin solid curves, and the approximation given by eq 37,  $\tilde{u}_e(h, \alpha, \xi, \eta_e)$ , is shown by dashed curves. The values of  $h$  correspond to the following distances between the surfaces of the nanotubes: (a,b,c)  $\delta h = h - 2R_T = 3.15 \text{ \AA}$ , (d,e,f)  $\delta h = 2.45 \text{ \AA}$ . The values of  $\alpha$  are (a,d)  $\alpha = 10^\circ$ , (b,e)  $\alpha = 30^\circ$ , (c,f)  $\alpha = 90^\circ$ . Curves 1–4 are shown for  $\eta_e = -15 \text{ \AA}$ ,  $\eta_e = -5 \text{ \AA}$ ,  $\eta_e = 5 \text{ \AA}$ , and  $\eta_e = 15 \text{ \AA}$ , respectively.

of the nanotube oriented along the  $\xi$ -axis and interacting with the semi-infinite nanotube is divided into  $N_\xi - 1$  equal subsegments of length  $\Delta\xi$ , with the ends of the subsegments defined as

$$\bar{\xi}_{(n)} = \xi_1 + \Delta\xi n, \quad \Delta\xi = \frac{\xi_2 - \xi_1}{N_\xi - 1},$$

$$n = 0, \dots, N_\xi - 1$$

The approximate interaction potential  $\tilde{U}_{\text{Se}}$  can then be calculated by applying, e.g., the trapezoidal rule to the integral in eq 38:

$$\tilde{U}_{\text{Se}}(h, \alpha, \xi_1, \xi_2, \eta_e) = \Delta\xi \Gamma(h, \alpha) \times$$

$$\left[ \frac{u_{\text{el}}(\bar{h}_{(0)}, \bar{\vartheta}_{(0)}) + u_{\text{el}}(\bar{h}_{(N_\xi-1)}, \bar{\vartheta}_{(N_\xi-1)})}{2} + \sum_{n=1}^{N_\xi-2} u_{\text{el}}(\bar{h}_{(n)}, \bar{\vartheta}_{(n)}) \right] \quad (39)$$

where

$$\bar{h}_{(n)} = \sqrt{h^2 + (\bar{\xi}_{(n)} \Omega(\alpha) \sin \alpha)^2}, \quad \bar{\vartheta}_{(n)} = \bar{\xi}_{(n)} \cos \alpha - \Theta(\alpha) \eta_e$$

The interaction potential  $\tilde{U}_{\text{Se}}$  given by eq 39 is expressed through two-dimensional functions  $\Gamma(h, \alpha)$  and  $u_{\text{el}}(h, \xi)$  and one-dimensional functions  $\Omega(\alpha)$  and  $\Theta(\alpha)$ . Similar to the potential for the interaction with an infinitely long nanotube, eq 25, the efficiency of the evaluation of  $\tilde{U}_{\text{Se}}$  can be improved by tabulating the values of the functions used in the calculation and using an interpolation of the tabulated values in the course of a dynamic simulation involving a large number of nanotubes (see section 4).

The result of the calculation of the approximate potential  $\tilde{U}_{\text{Se}}(h, \alpha, \xi_1, \xi_2, \eta_e)$  for (5,5), (10,10), and (20,20) single-walled CNTs is shown and compared with the true potential  $U_{\text{Se}}(h, \alpha, \xi_1, \xi_2, \eta_e)$  in Figure 10. The potentials are plotted as functions of the position of the end of the semi-infinite nanotube for fixed coordinates of the nanotube segment ( $\xi_1 = -10 \text{ \AA}$ ,  $\xi_2 = 10 \text{ \AA}$ ) and several values of intertube distance  $h$  and angle  $\alpha$ . The number of points  $N_\xi$  used in the numerical integration in eq 39 is equal to 100. The values of  $\tilde{U}_{\text{Se}}$  obtained with  $N_\xi = 10$ , however, are found to be very close to the ones shown in the figure. The approximate potential  $\tilde{U}_{\text{Se}}$  is found to provide a good quantitative approximation for  $U_{\text{Se}}$  in the entire range of geometric parameters and nanotube radii considered in this study. The maximal discrepancy between the approximate and true potentials,  $|\tilde{U}_{\text{Se}} - U_{\text{Se}}|$ , is less than 6% for the data shown in Figure 10.

The shapes of the curves shown in Figure 10 vary gradually with angle  $\alpha$  and the radius of the nanotube but remain qualitatively similar for a fixed intertube separation. All of the curves calculated for  $\delta h = 2.45 \text{ \AA}$  have a maximum at  $\eta_e < 0$  and a minimum at  $\eta_e > 0$ , Figure 10a–c. The positions of the minimum and maximum shift to  $\eta_e \approx \xi_2$  and  $\eta_e \approx -\xi_2$ , respectively, as the segment and the nanotube align with each other and become parallel (curve 1). In the case of parallel nanotubes, the presence of the extrema is a direct consequence of the presence of the corresponding extrema in the distributions of the potential density for parallel nanotubes shown in Figure 2b (curves 1–5). For larger separations, e.g.,  $\delta h = 3.15 \text{ \AA}$  in Figure 10d–f, the attraction between the nanotube and the segment plays the dominant role and the potential exhibits a

monotonous decrease as the segments are moved in the positive direction of the  $\eta$ -axis. For parallel nanotubes, this behavior of the potential corresponds to the monotonous variation of the potential density in Figure 2b (curves 6 and 7).

#### 2.4. Radius-Independent Form of the Tubular Potential.

The approximate tubular potential defined by eqs 25 and 39 is capable of computationally efficient description of nonbonding interactions between nanotubes of arbitrary length and orientation. All of the parameters of the potential are defined by the interatomic potential  $\varphi(r)$ , surface density of atoms  $n_\sigma$ , and radius of nanotubes  $R_T$ . The explicit dependence of the potential on the radius of nanotubes can be considered as a shortcoming of the potential, as it is necessary to generate separate tables of two-dimensional functions  $\Phi(h, \zeta)$  and  $u_{\text{el}}(h, \xi)$  for every particular radius of nanotubes of interest.

The fact that the shapes of the dependences of potentials  $\tilde{U}_{\text{Se}}$  and  $\tilde{U}_{\text{Se}}$  on different geometric parameters (Figures 7 and 10) remain qualitatively similar for nanotubes of different radii, however, suggests that it may be possible to reformulate the potentials in a form where the radius dependence is accounted for analytically and the two-dimensional tables are built for reduced radius-independent geometrical parameters. Indeed, it has been demonstrated in refs 26 and 27 that it is possible to design an approximate interaction potential for parallel infinitely long nanotubes in terms of reduced parameters that make the potential to be independent of the radius of the nanotubes. Following this idea, the potentials  $\tilde{U}_{\text{Se}}$  and  $\tilde{U}_{\text{Se}}$  can be reformulated (without any additional approximations) in terms of tabulated functions that are independent of  $R_T$ . Such a reformulation is possible for interatomic potentials that can be expressed in the form of a linear combination of homogeneous functions, such as  $\varphi(r) = \varphi_{(n)}(r) - \varphi_{(m)}(r)$ , where  $\varphi_{(k)}(ar) = a^{-k} \varphi_{(k)}(r)$  and  $k = n, m$ . The Lennard-Jones potential without a cutoff (i.e., when  $C(r) = 1$  in eq 1) belongs to this class of potentials, with  $\varphi_{(k)}(r) = 4\epsilon(\sigma/r)^k$ , where  $k$  is equal to 12 and 6.

The potential density for two infinitely long parallel nanotubes of the same radius  $R_T$ , given by eq 10, can be rewritten for the Lennard-Jones interatomic potential without a cutoff in the following form:

$$u_{\infty}(h) = \frac{n_\sigma^2}{R_T^9} f_{\infty(12)}\left(\frac{h}{R_T}\right) - \frac{n_\sigma^2}{R_T^3} f_{\infty(6)}\left(\frac{h}{R_T}\right) \quad (40)$$

where functions

$$f_{\infty(k)}(h') = \int_0^{2\pi} \int_{-\infty}^{+\infty} \int_0^{2\pi} \varphi_{(k)}(r'(h', \phi_1, \eta', \phi_2)) d\phi_2 d\eta' d\phi_1 \quad (41)$$

are independent of the radius of the nanotubes and  $h' = h/R_T$ ,  $\eta' = \eta/R_T$ , and  $r' = r/R_T$ . Subsequently, the function  $\Phi(h, \zeta)$  in eq 23 can be rewritten in terms of radius-independent functions as follows:

$$\Phi(h, \zeta) = \frac{n_\sigma^2}{R_T^8} \Phi_{(12)}\left(\frac{h}{R_T}, \frac{\zeta}{R_T}\right) - \frac{n_\sigma^2}{R_T^2} \Phi_{(6)}\left(\frac{h}{R_T}, \frac{\zeta}{R_T}\right) \quad (42)$$

where

$$\Phi_{(k)}(h', \zeta') = \text{sgn}(\zeta') \int_{\zeta'_{\min}(h')}^{\zeta'^1} f_{\text{sc}(k)}(\sqrt{h'^2 + \zeta'^2}) d\zeta' \quad (43)$$

The radius-independent functions  $\Phi_{(k)}(h', \zeta')$  can be calculated with eq 43 only once and then used in the tabulated form (instead of the radius-dependent function  $\Phi(h, \zeta)$  given by eq 23) for calculation of the interaction potential for an arbitrary  $R_T$ . The dependence of the potential on the radius of nanotubes is accounted for by scaling of arguments of  $\Phi_{(k)}(h', \zeta')$  and by radius-dependent coefficients in eq 42, as well as by the radius-dependent scaling functions  $\Gamma(h, \alpha)$  and  $\Omega(\alpha)$  in eq 25. A similar

approach can be used to rewrite the potential for semi-infinite nanotube ( $\tilde{U}_{\text{Se}}$  given by eq 39) in a form where the two-dimensional function  $u_{\text{el}}(h, \xi)$  is expressed through universal functions independent of the radius of nanotubes.

As a practical note, the calculation of the potentials expressed through radius-independent functions/tables requires longer computer time and more computer memory as compared with their evaluation in the radius-dependent form. Moreover, the requirement that the interatomic potential  $\varphi(r)$  should be a linear combination of homogeneous functions prevents the introduction of a cutoff function that brings the potential  $\varphi(r)$  and its derivatives to zero at a constant cutoff distance  $r_c$  that is

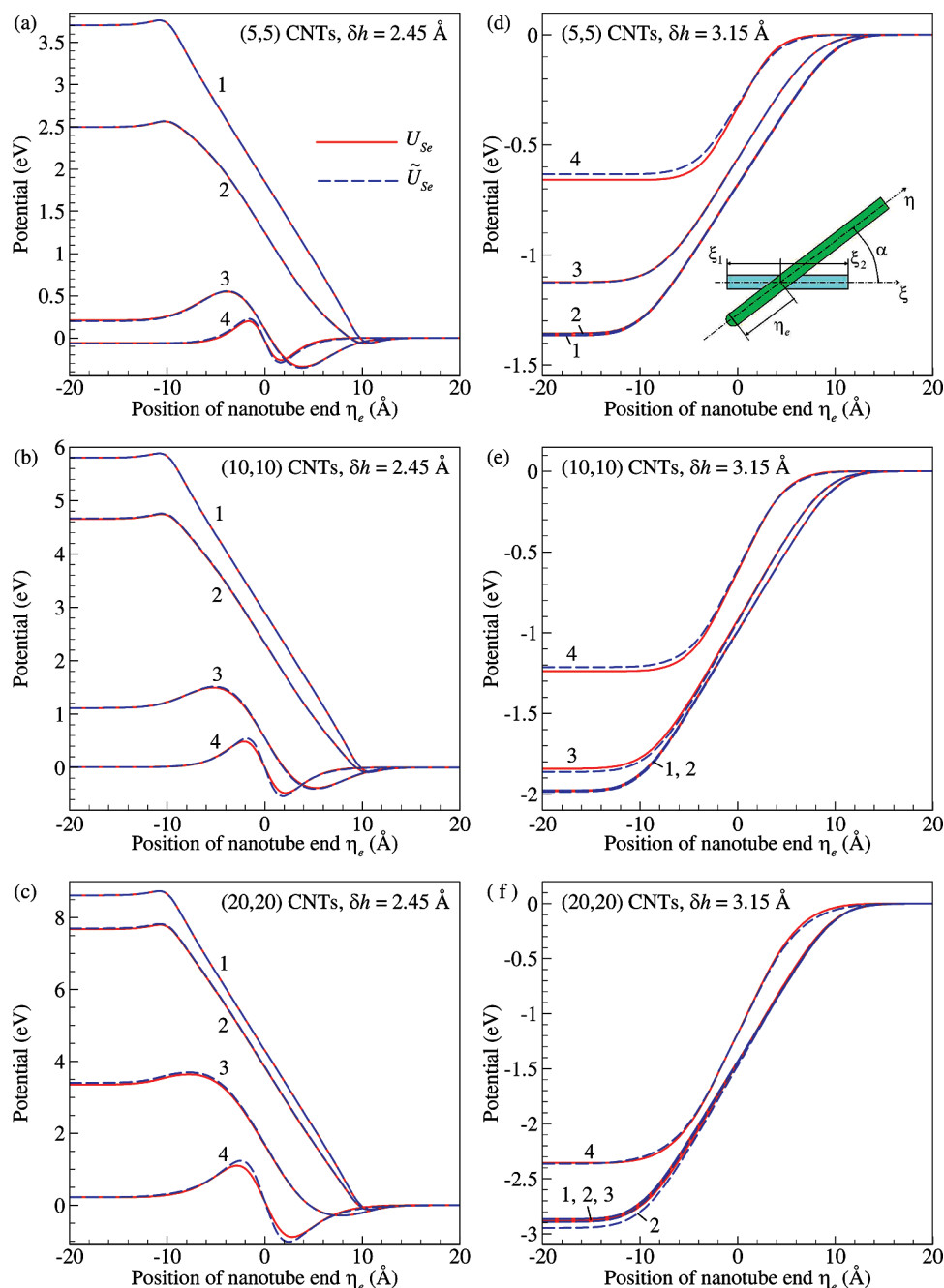


**Figure 10.** True and approximate potentials for interaction between a semi-infinite single-walled CNT with a nanotube segment. The true potential  $U_{\text{Se}}(h, \alpha, \xi_1, \xi_2, \eta_e)$  (solid curves, eqs 3–5) and the approximate potential  $\tilde{U}_{\text{Se}}(h, \alpha, \xi_1, \xi_2, \eta_e)$  (dashed curves, eq 39) are shown as functions of the position of the end of the semi-infinite nanotube,  $\eta_e$ . The calculations are performed for constant values of coordinates of the segment ends ( $\xi_1 = -10$  Å,  $\xi_2 = 10$  Å), two distances between the surfaces of the nanotubes,  $\delta h = h - 2R_T = 2.45$  Å (a–c) and  $\delta h = 3.15$  Å (d–f), and three types of single-walled CNTs, (5,5) (a,d), (10,10) (b,e), and (20,20) (c,f). Curves 1–4 are shown for  $\alpha = 0^\circ$ ,  $\alpha = 10^\circ$ ,  $\alpha = 30^\circ$ , and  $\alpha = 90^\circ$ , respectively.

independent of  $R_7$ . The application of the potential for large-scale simulations involving large ensembles of nanotubes would require application of the cutoff directly to the tubular potential given by eqs 25 and 39, hampering the direct mapping between the atomistic and mesoscopic potentials.

### 3. Force and Torque Acting on Nonparallel Nanotubes

The approximate tubular potential introduced in the previous section enables a straightforward analysis of forces acting on straight nanotubes interacting with each other. Two examples considered below are for the interaction between two infinitely long nanotubes and an infinitely long nanotube and a finite-length nanotube. Starting with the two infinitely long nanotubes and considering  $0^\circ < \alpha < 180^\circ$ , the interaction energy  $\tilde{U}_{\infty\infty}(h, \alpha)$ , translational force  $F_{\infty}(h, \alpha)$ , and torque  $T_{\infty}(h, \alpha)$  (below we consider the force and torque acting in the direction of the  $Ox$  axis in Figure 1a on the nanotube placed along the  $\eta$ -axis) can be derived from eq 25:

$$\tilde{U}_{\infty\infty}(h, \alpha) = \lim_{\substack{\xi_1 \rightarrow -\infty \\ \xi_2 \rightarrow +\infty}} \tilde{U}_{S\infty}(h, \alpha, \xi_1, \xi_2) = 2 \frac{\Gamma(h, \alpha)}{\Omega(\alpha) \sin \alpha} \Phi_{\infty}(h) \quad (44)$$

$$F_{\infty}(h, \alpha) = -\frac{\partial \tilde{U}_{\infty\infty}}{\partial h} = -\Psi(h, \alpha) \tilde{U}_{\infty\infty}(h, \alpha) \quad (45)$$

$$T_{\infty}(h, \alpha) = -\frac{\partial \tilde{U}_{\infty\infty}}{\partial \alpha} = -\Lambda(h, \alpha) \tilde{U}_{\infty\infty}(h, \alpha) \quad (46)$$

where

$$\Phi_{\infty}(h) = \lim_{\zeta \rightarrow +\infty} \Phi(h, \zeta) \quad (47)$$

$$\Psi(h, \alpha) = \frac{1}{\Gamma(h, \alpha)} \frac{\partial \Gamma}{\partial h} + \frac{1}{\Phi_{\infty}(h)} \frac{d\Phi_{\infty}}{dh} \quad (48)$$

$$\Lambda(h, \alpha) = \frac{1}{\Gamma(h, \alpha)} \frac{\partial \Gamma}{\partial \alpha} - \frac{1}{\Omega(\alpha)} \frac{d\Omega}{d\alpha} - \frac{\cos \alpha}{\sin \alpha} \quad (49)$$

The values and behavior of functions  $\Psi(h, \alpha)$  and  $\Lambda(h, \alpha)$  are largely defined by their last terms,  $(1/\Phi_{\infty}) d\Phi_{\infty}/dh$  and  $-\cot \alpha$ , respectively, with other terms making minor contributions (see analysis given below for (10,10) CNTs). Therefore, the force and torque can be approximated by the following simple equations:

$$F_{\infty}(h, \alpha) \approx -2 \frac{\Gamma(h, \alpha)}{\Omega(\alpha) \sin \alpha} \frac{d\Phi_{\infty}(h)}{dh} \quad (50)$$

$$T_{\infty}(h, \alpha) \approx \cot \alpha \tilde{U}_{\infty\infty}(h, \alpha) = 2 \frac{\Gamma(h, \alpha) \cot \alpha}{\Omega(\alpha) \sin \alpha} \Phi_{\infty}(h) \quad (51)$$

Since the expression  $\Gamma(h, \alpha)/(\Omega(\alpha) \sin \alpha)$  is positive for any  $0^\circ < \alpha < 180^\circ$ , the direction of the force is defined by the sign of the derivative  $d\Phi_{\infty}/dh$ . This implies that the direction of the force is independent of the angle  $\alpha$  and, for a given type/radius of the nanotubes, is uniquely defined by the distance  $h$ . The

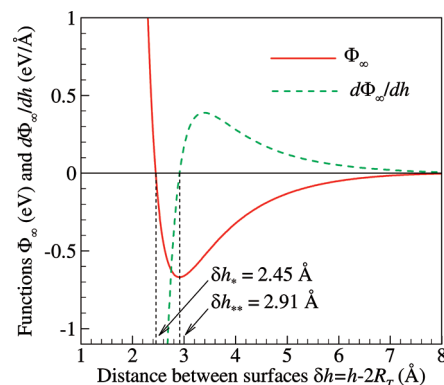


**Figure 11.** Function  $\Phi_{\infty}(h)$  defined by eqs 47 and 23 and its derivative  $d\Phi_{\infty}/dh$  calculated for (10,10) single-walled CNTs. The distance between the surfaces of the nanotubes,  $\delta h = h - 2R_7$ , is used as an argument of the function. The values of the intertube distance, where  $\Phi_{\infty}(h)$  and its derivative are zero and change their signs, are marked on the figure as  $\delta h^*$  and  $\delta h^{**}$ , respectively.

torque changes its direction at  $\alpha = 90^\circ$ , but for both  $\alpha < 90^\circ$  and  $\alpha > 90^\circ$ , the direction of the torque is defined by the sign of  $\Phi_{\infty}(h)$ , i.e., is also uniquely defined by the distance  $h$ .

For (10,10) single-walled CNTs, the function  $\Phi_{\infty}(h)$  and its derivative are plotted in Figure 11. The function  $\Phi_{\infty}(h)$  changes its sign at  $\delta h^* = 2.45 \text{ \AA}$  (i.e.,  $\Phi_{\infty}(2R_7 + \delta h^*) = 0$ ), while its derivative changes its sign at  $\delta h^{**} = 2.91 \text{ \AA}$ . The negative values of  $\Phi_{\infty}(h)$  at  $\delta h > \delta h^*$  correspond to the negative torque for  $0^\circ < \alpha < 90^\circ$  and positive torque for  $90^\circ < \alpha < 180^\circ$ , which in both cases acts to align the nanotubes parallel to each other. The positive values of  $\Phi_{\infty}(h)$  at  $\delta h < \delta h^*$ , on the contrary, correspond to the torque that acts to orient the nanotubes perpendicular to each other. Similarly, the translational force given by eq 50 is positive (repulsive) at  $\delta h < \delta h^{**}$  and negative (attractive) at  $\delta h > \delta h^{**}$ . The observation that  $\delta h^* < \delta h^{**} < \delta h_0$ , where  $\delta h_0 = 3.144 \text{ \AA}$  is the equilibrium separation of parallel nanotubes, indicates that in CNT-based materials experiencing moderate or no external pressure the torque acting on nanotubes due to intertube interactions would make them align with each other, providing the driving force for spontaneous self-assembly of CNTs into bundles observed in experiments.<sup>1-3,5-10</sup> At large values of pressure, however, when typical separation between nanotubes becomes smaller than  $\delta h^*$ , the formation of bundles can be suppressed, as suggested by the reversed direction of the torque.

Equation 50 implies that for infinitely long nonparallel nanotubes ( $\sin \alpha \neq 0$ ) the equilibrium separation between the tubes is equal to  $\delta h^{**}$ . For nanotubes that are parallel to each other ( $\sin \alpha = 0$ ), on the other hand, the equilibrium separation is defined by the position  $\delta h_0$  of the minimum of the potential density  $u_{\infty\parallel}(h)$  (see dashed curve in Figure 2a). Since  $\delta h^{**} \neq \delta h_0$ , the dependence of the equilibrium separation on  $\alpha$  has a singularity at  $\sin \alpha = 0$ , which is a consequence of the corresponding singularity of the potential  $\tilde{U}_{S\infty}$  (eq 25) applied to infinitely long nanotubes at  $\xi_2 = -\xi_1 \rightarrow \infty$ .

The dependences of the force and torque on the angle  $\alpha$ , predicted by eqs 50 and 51, are shown in Figures 12a and 13a for several intertube separations between two infinitely long (10,10) single-walled CNTs. Both force and torque are monotonous functions of  $\alpha$ , with the magnitudes of the force and torque increasing with decreasing angle and tend to infinity as  $\sin \alpha \rightarrow 0$ . This behavior is expected, since the interaction energy of two infinitely long parallel nanotubes is infinity.

To justify the approximations (omission of the first term in eq 48 and the first two terms in eq 49) used in formulating the

simplified expressions for the force and torque given by eqs 50 and 51, the accuracy of the approximations is analyzed here for data shown in Figures 12a and 13a. The relative differences between  $(1/\Phi_\infty) d\Phi_\infty/dh$  and  $\Psi(h,\alpha)$  (and, consequently, between the values of the force  $F_\infty(h,\alpha)$  predicted by eqs 50 and 45) is less than 5% in the whole range of values of  $h$  and  $\alpha$  used in the calculations. The relative differences between  $-\cot \alpha$  and  $\Lambda(h,\alpha)$  (and, consequently, between the values of the torque  $T_\infty(h,\alpha)$  predicted by eqs 51 and 46) is illustrated in the inset in Figure 13b. The relative difference is less than 5% for  $\alpha < 50^\circ$ , while for larger angles it increases up to  $\sim 15\%$ . The absolute values of  $\Lambda(h,\alpha)$  and  $T_\infty(h,\alpha)$ , however, are close to zero at large angles, where the relative difference between  $-\cot \alpha$  and  $\Lambda(h,\alpha)$  increases. As a result, the dependences predicted by eqs 45 and 46, if shown in Figures 12a and 13a, would visually coincide with the curves calculated with eqs 50 and 51.

The force and torque acting on an infinitely long nanotube that interacts with a segment of a finite length  $L$  exhibit more complex dependences on the geometric parameters. If the finite-length nanotube is positioned symmetrically with respect to the axis  $Ox$  ( $\xi_1 = -\xi_2$ ,  $\eta_1 \rightarrow \infty$ , and  $\eta_2 \rightarrow \infty$  in Figure 1a), the translational force and the torque can be obtained by differentiation of potential  $\tilde{U}_{S_\infty}(h,\alpha,\xi_1,\xi_2)$  given by eq 25:

$$F(h, \alpha, L) = -\frac{\partial \tilde{U}_{S_\infty}}{\partial h}(h, \alpha, -L/2, L/2) \quad (52)$$

$$T(h, \alpha, L) = -\frac{\partial \tilde{U}_{S_\infty}}{\partial \alpha}(h, \alpha, -L/2, L/2) \quad (53)$$

The dependences of the force and torque on the angle  $\alpha$ , predicted by eqs 52 and 53 for  $L = 100 \text{ \AA}$ , are shown in Figures 12b and 13b. For large  $\alpha$ , when the ends of the nanotube are beyond the cutoff distance for the intertube interaction, the values of the force and torque coincide with the corresponding values for infinitely long nanotubes. For smaller angles, however, the angular dependences start to deviate from the case of infinitely long nanotubes. For data shown in Figures 12b and 13b, the difference in force and torque predicted for finite ( $L = 100 \text{ \AA}$ ) and infinitely long nanotubes exceeds 1% at an angle of about  $18^\circ$ , whereas the same deviation for a 10 times longer segment ( $L = 1000 \text{ \AA}$ ) is observed at a much smaller angle of  $2^\circ$ .

The differences between the angular dependence observed for the finite and infinitely long nanotubes at small angles in Figures 12 and 13 are related to the difference in the asymptotic behavior of the corresponding equations at  $\sin \alpha \rightarrow 0$ . The

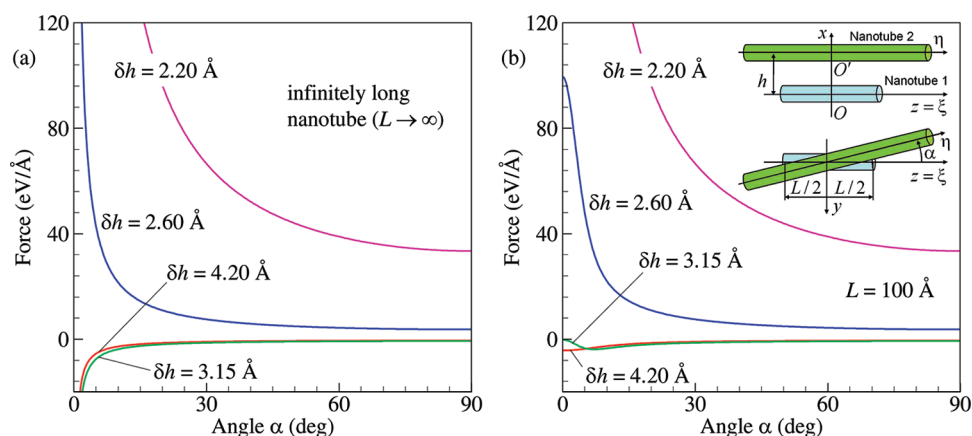


**Figure 12.** Translational force acting on an infinitely long (10,10) single-walled CNT (nanotube 2 in the inset) interacting with a CNT of the same type and length  $L$  (nanotube 1 in the inset) shown as a function of the angle  $\alpha$  between the nanotubes for several values of the distance between the surfaces of the nanotubes,  $\delta h = h - 2R_T$ . Nanotube 1 is assumed to be infinitely long in panel a and has a length of  $L = 100 \text{ \AA}$  in panel b. The inset in panel b shows the side and top views of the geometrical configuration of the system.

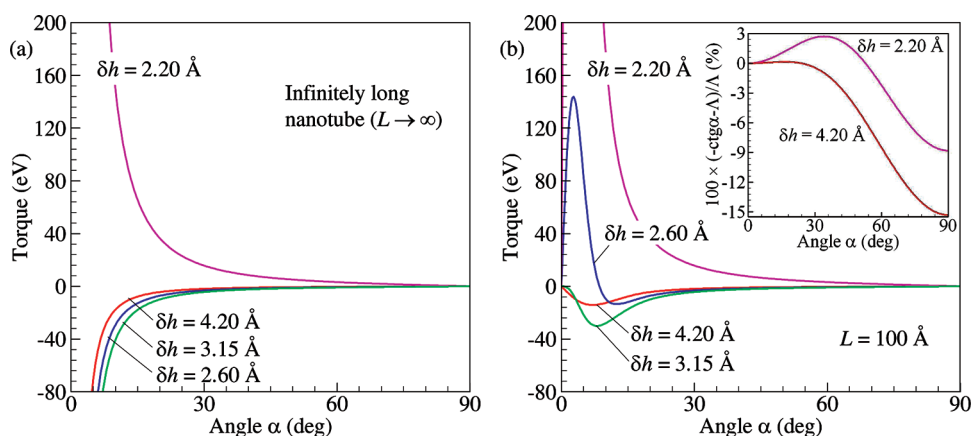


**Figure 13.** Torque acting on an infinitely long (10,10) single-walled CNT (nanotube 2 in the inset in Figure 12b) interacting with a CNT of the same type and length  $L$  (nanotube 1 in the inset in Figure 12b) shown as a function of the angle  $\alpha$  between the nanotubes for several values of the distance between the surfaces of the nanotubes,  $\delta h = h - 2R_T$ . Nanotube 1 is assumed to be infinitely long in panel a and has a length of  $L = 100 \text{ \AA}$  in panel b. The relative position of the nanotubes is shown in the inset in Figure 12b. The inset in panel b shows the relative difference between function  $\Lambda(h,\alpha)$  defined by eq 49 and its approximation by  $-\cot \alpha$ .

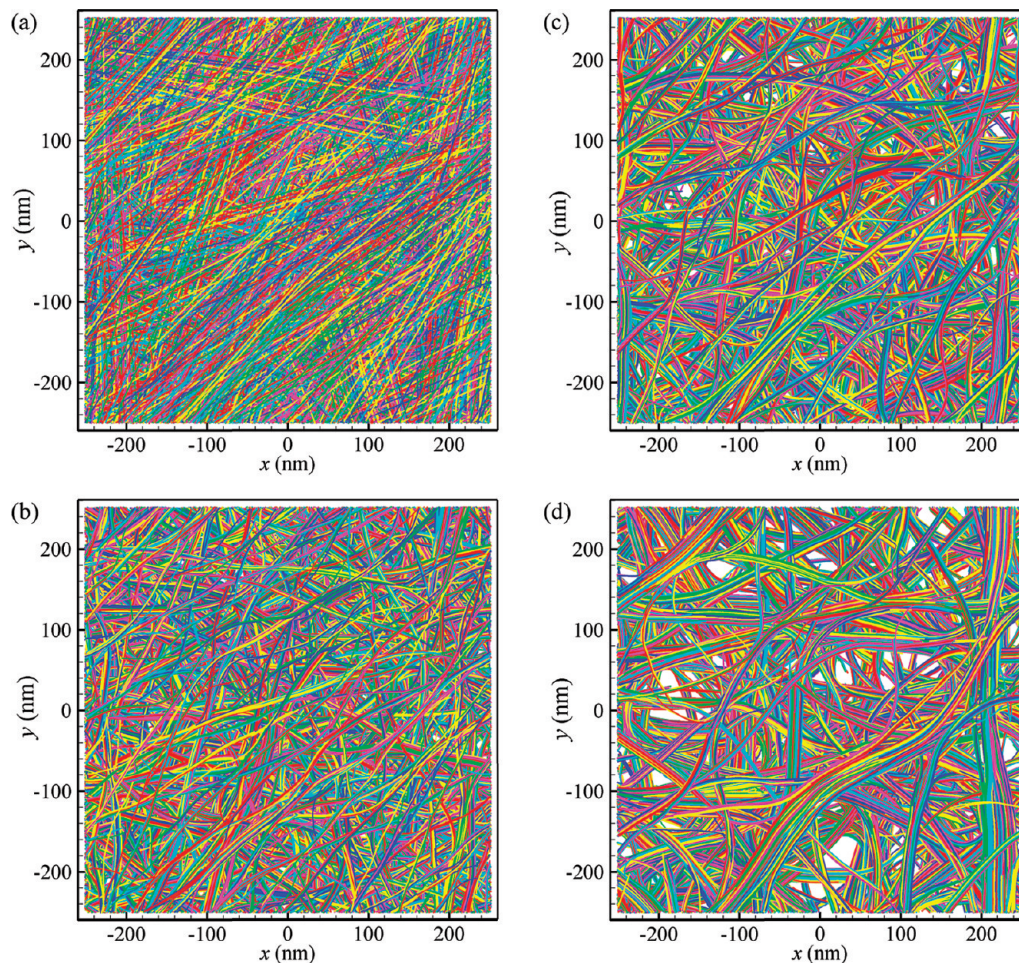


**Figure 14.** Snapshots from a constant-volume mesoscopic simulation performed with the tubular potential for a system of 4050 (10,10) single-walled CNTs. The length of each CNT is 400 nm, the dimensions of the system are 500 nm  $\times$  500 nm  $\times$  100 nm, and the density of the system is 0.2 g/cm<sup>3</sup>. The initial sample shown in panel a is composed of layers of straight randomly dispersed nanotubes. The snapshots taken during the dynamic simulation are shown for times of 0.5 ns (b), 1 ns (c), and 2 ns (d). The simulation is performed under constant total energy conditions during the first nanosecond and under constant 300 K temperature at later time. Different colors correspond to different individual CNTs.

torque, in particular, approaches zero for a finite-length nanotube and tends to infinity for the infinitely long nanotube. This leads to a nonmonotonous dependence of the torque on  $\alpha$  observed for finite-length nanotubes at any intertube separation (Figure 13b). For small distances between the nanotubes, when the repulsion dominates, the torque acting to misalign the nanotubes increases at small angles and then drops to zero as  $\sin \alpha \rightarrow 0$ . The parallel orientation of the nanotubes corresponds to a state of unstable equilibrium in these cases. For intermediate separations, in the vicinity of  $\delta h_*$ , the angular dependence of torque exhibits a more complex behavior, with both minimum and maximum present and the direction of torque changing with  $\alpha$ . In these cases, the equilibrium angle (when the torque is zero) is no longer equal to 0 or 90°; e.g., for  $\delta h = 2.6 \text{ \AA}$ , it is equal to 8.6° (Figure 13b). The translational force acting on the finite-size nanotube tends to finite values at  $\sin \alpha \rightarrow 0$  and can also exhibit nonmonotonous dependences on  $\alpha$ , albeit only for a narrow range of intertube separations in the vicinity of the equilibrium separation  $\delta h_0$  (Figure 12b). In contrast to the case of infinitely long nanotubes, for finite  $L$ , the equilibrium distance between the nanotubes depends on  $\alpha$ . The equilibrium distance approaches  $\delta h_0$  for  $\sin \alpha \rightarrow 0$ , and becomes close to  $\delta h_{**}$  for larger angles and sufficiently large  $L$ .

#### 4. Mesoscopic Simulation of Self-Assembly of CNTs into Bundles

The development of the mesoscopic tubular potential described in section 2 opens up a new direction in the computational analysis of CNT-based materials, with the main area of prospective applications being in dynamic simulations of systems consisting of a large number of interacting nanotubes. To illustrate the ability of the tubular potential to provide a computationally efficient description of nonbonding interactions in CNT-based materials, in this section, we present the results of a simulation of the structural self-organization in a system containing thousands of interacting nanotubes.

The dynamic simulation is performed with a mesoscopic model in which nanotubes are represented as chains of cylindrical segments.<sup>11</sup> Each segment is defined by coordinates of its ends (or nodes). The dynamics of a system of interacting CNTs is described by the equations of motion of classical mechanics solved for the positions of the nodes. The forces acting on the nodes are calculated on the basis of the mesoscopic force field that consists of internal and external parts. The internal part of the force field accounts for the stretching, bending, and torsional deformations of individual nanotubes and is described in ref 11. The external part of the force field represents intertube

interactions and is described by the tubular potential as briefly explained below.

The most straightforward approach to using the tubular potential for calculation of the intertube van der Waals interaction energies and forces would be to apply the potential for segment–segment interaction  $U_{SS}(h, \alpha, \xi_1, \xi_2, \eta_1, \eta_2)$  given by eq 7 to every pair of interacting segments. This approach would involve double evaluation of potential  $\tilde{U}_{Se}$  for each pair of segments. The calculation of  $\tilde{U}_{Se}$ , however, involves numerical integration of potential density  $u_{e||}$  (see eqs 38 and 39) and is computationally expensive. The computational efficiency of the calculations can be significantly enhanced if calculation of  $\tilde{U}_{Se}$  is replaced, whenever possible, by calculation of  $\tilde{U}_{S\infty}$ . The evaluation of  $\tilde{U}_{S\infty}$  with eq 25 does not involve a numerical integration and can be efficiently performed using prerecorded tables of functions  $\Gamma_{\perp}(h)$  and  $\Phi(h, \zeta)$ . In order to ensure the accuracy of the representation of interactions between curved nanotubes and to improve the total energy conservation in dynamic simulations, a special weighted approach that accounts for the local curvatures of the interacting nanotubes is also developed<sup>48,49</sup> and applied in the simulation described below. The derivation of the equations for forces acting between nanotubes that interact with each other through the tubular potential are presented in section S2 of the Supporting Information in the form suitable for a straightforward implementation in a computer code.

The simulation is performed for a system consisting of 4050 (10,10) 400 nm long single-walled CNTs, with each nanotube represented by 200 segments with an equal equilibrium length of 2 nm. The initial configuration shown in Figure 14a is generated by stacking thin layers of straight nanotubes with a distance between the layers that ensures the interlayer interaction. This method has been found to be capable of producing systems with a high degree of randomness in CNT positions and orientations, and with densities as high as 0.6 g/cm<sup>3</sup>.<sup>50</sup> The dimensions of the computational system used in this work are 500 nm × 500 nm × 100 nm, and the average density is 0.2 g/cm<sup>3</sup>. The periodic boundary conditions are applied in the lateral directions (along the *x*- and *y*-axes). The volume of the system is maintained constant during the simulation by two planes enclosing the CNT film from the two sides in the *z* direction and interacting with the nanotubes by a short-range repulsive potential.

The evolution of the system in the dynamic simulation is illustrated by the snapshots shown in Figure 14b–d. Although the velocities of all nodes in the initial configuration are set to zero, the interaction among nanotubes triggers spontaneous rearrangement of the configuration to a complex continuous network of CNT bundles. The formation of bundles reduces the potential energy of intertube interactions and, as a result, increases the kinetic energy of the dynamic system. The absence of the high-frequency atomic vibrations in the model prevents dissipation of the kinetic energy into the internal energy of the nanotubes, leading to the fast increase in the “temperature” associated with the dynamic degrees of freedom of the model in the dynamic simulation conserving the total energy. In order to partially account for the dissipation of the kinetic energy released in the process of self-organization of the nanotubes into bundles, a temperature control is introduced after the first nanosecond of the simulation. The temperature of the dynamic degrees of freedom is maintained in this case at 300 K by scaling the velocities of the nodes according to the Berendsen thermostat method<sup>51</sup> commonly used in atomistic molecular dynamics simulations. Despite the significant slowdown of the structural

changes in the system after the first nanosecond, the evolution of the structure continues under the constant temperature conditions. The primary direction of the long-term structural evolution is the coarsening of the bundles, which proceeds by thin bundles and remaining individual nanotubes joining the thicker bundles, Figure 14d. The observation of the continuing changes in the system at the constant-temperature stage of the simulation is consistent with experimental observations of relatively large vibrations of CNTs caused by thermal fluctuations at room temperature.<sup>52</sup>

The structure of the random network of bundles (Figure 15a) obtained in the simulation is similar to the ones observed in experimental images of the surface of CNT mats or “bucky paper”.<sup>2,3,5–10</sup> The diameter of CNT bundles in Figures 14d and 15a ranges from 2 to 30 nm with few thicker bundles. By changing the simulation conditions, structures with smaller and larger bundles can be obtained in the simulations. The range of the bundle diameters is consistent with experimental observations, with the reported ranges of the bundle diameter being from 5 to 20 nm (ref 1), from 2 to 34 nm (ref 8), from 1 to 30 nm (ref 9), or from 30 to 60 nm (ref 7). A detailed analysis of the arrangement of individual nanotubes in the network of bundles reveals several characteristic structural features that can be more clearly seen in the enlarged view of a section of the simulated system shown in Figure 15b. These features, also observed in experimental images,<sup>3,6,7,9,10</sup> include splitting of a thick bundle into two or more thinner ones and interconnections formed by nanotubes that belong to two different bundles.

Although the packing of nanotubes in bundles just after their formation is rather irregular, the long-term rearrangement of nanotubes at 300 K results in a gradual increase of their ordering in the bundles, with local hexagonal arrangements appearing in the cross sections of the bundles, e.g., Figure 15c. The hexagonal arrangement of CNTs in bundles corresponds to the minimum of the potential energy of intertube interaction and has been observed in experiments.<sup>1,2</sup> Since the bundles are highly interconnected with each other and form a continuous random network, there is a relatively small number of bundles that end inside the material. This characteristic of the simulated CNT material is consistent with experiments where the bundles in CNT network structures are characterized as “truly endless”.<sup>53</sup> In the rare cases when bundle ends are observed, however, the nanotubes constituting such bundles tend to align their ends with each other. The alignment of CNT ends reduces the intertube interaction energy and is also in agreement with experimental observations.<sup>1</sup>

## 5. Conclusions and Outlook

A compact and computationally efficient mesoscopic tubular potential is developed for the description of interactions between CNTs of arbitrary lengths and orientations. The potential is formulated within a general continuum description of the van der Waals intertube interactions based on the integration of an interatomic potential over the surfaces of the interacting nanotubes. The tubular potential reduces the functional dependence of the potential energy on six independent geometric variables to a combination of several functions, each depending on only one or two geometric parameters. These functions can be tabulated and used in a computationally efficient algorithm enabling dynamic simulations of systems composed of thousands of CNTs. The tubular potential is completely defined by the functional form and parameters of the carbon–carbon interatomic potential for nonbonded interactions and gives an excellent accuracy in reproducing the results of the direct

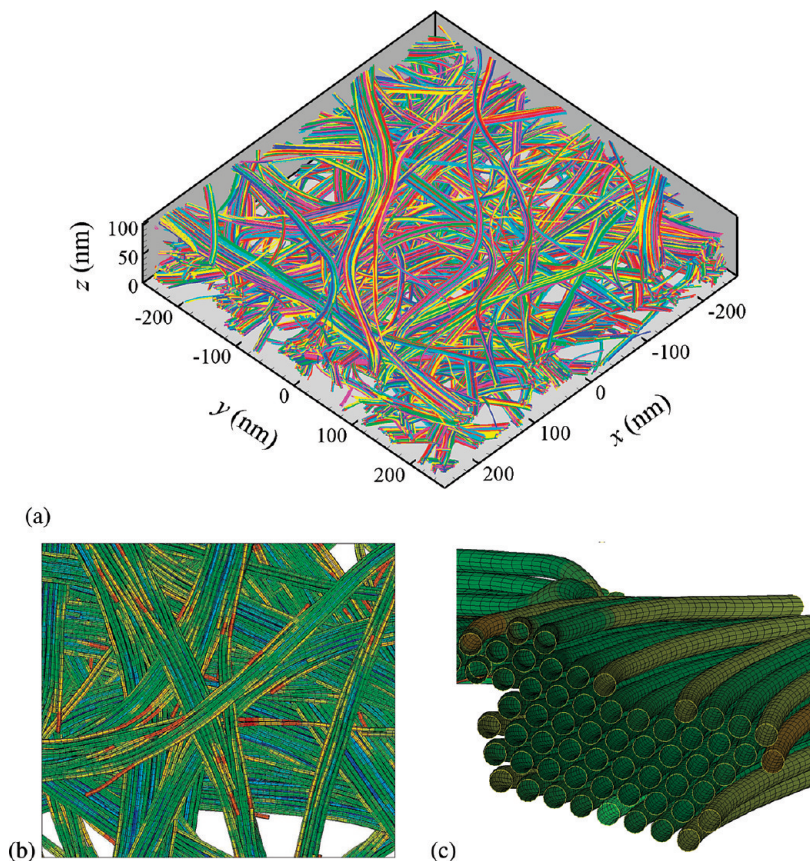


**Figure 15.** Three-dimensional view of the final configuration obtained in the simulation illustrated in Figure 14d, an enlarged view of a part of the network of bundles generated in this simulation (b), and a cross-section of a typical bundle (c). Different nanotubes are colored by different color in panel a, whereas in panel b the nanotubes are colored according to the local intertube interaction energy, from blue and green corresponding to a low energy realized for parallel tubes in a bundle to red corresponding to a higher energy of nanotube segments that have a weak interaction with other nanotubes.

numerical integration over the surfaces of nanotubes, albeit for a tiny fraction of the computational cost. For interatomic potentials that can be represented as a linear combination of homogeneous functions, such as the Lennard-Jones potential without a cutoff function, the tubular potential can be expressed in terms of universal functions independent of the radius of the nanotubes without any additional approximations.

The relatively simple functional form of the tubular potential makes it possible to perform analytical analysis of the energy and forces acting on a pair of interacting CNTs. The results of the analysis reveal a complex dependence of the interaction energy, translational force, and torque on the intertube separation and angle characterizing the relative orientation of the nanotubes. The direction of torque, in particular, is found to depend on the distance between the nanotubes, with the torque acting to align the nanotubes parallel to each other at large distances, when attraction between the nanotubes plays the dominant role, and acting to orient the nanotubes perpendicular to each other at small distances. This observation suggests that intertube interactions favor alignment of nanotubes and their self-assembly into bundles in the absence of external pressure.

The main area of prospective application of the tubular potential, however, is likely to be not in the analytical investigation of the potential energy surface in the space of geometric parameters but in mesoscopic dynamic simulations of systems consisting of a large number of interacting nanotubes. In particular, a mesoscopic model for CNTs based on the developed tubular potential describing the van der Waals interactions is used in this work to study the structural evolution

in a system of 4050 nanotubes for nanoseconds. The initial system composed of randomly distributed and oriented CNTs is predicted to spontaneously self-assemble into a continuous network of bundles with partial hexagonal ordering of CNTs in the bundles. The structure of the network of interconnected CNT bundles produced in the simulation is similar to the structures observed in experimental images of CNT films and “bucky paper”. With the length of each nanotube being 400 nm, an atomic-level representation of a similar system of 4050 nanotubes would involve more than 2.5 billion carbon atoms, making atomistic simulation unfeasible. In the mesoscopic simulation, on the other hand, the same system is described by  $\sim 8 \times 10^5$  dynamic nodes, allowing for the simulation to be completed with moderate computing resources, e.g., on a single workstation.

The development of the tubular potential creates a solid foundation for further advancement of the mesoscopic force field model that would broaden the range of potential applications of the dynamic mesoscopic model. The general framework of the mesoscopic model is sufficiently flexible to allow for an extension to modeling of single-walled CNTs of different radii and multiwalled CNTs, representation of buckling, fracture, and dynamic variation of radii, as well as incorporation of dissipative forces and an approximate description of the internal energy of nanotubes associated with high-frequency atomic vibrations. These features of the model can be added as needed for addressing particular aspects of the behavior of CNT-based materials, such as material response to dynamic loading or thermal transport properties.

Although in this work the mesoscopic tubular potential is developed and parametrized for single-walled CNTs, it can be easily adopted for multiwalled CNTs, where the interaction potential can be found by summing the contributions from each of the concentric tubes constituting the multiwalled CNTs.<sup>28</sup> Moreover, the general procedure for designing the potential is not limited to CNTs or graphitic structures. The tubular potential can be parametrized for an arbitrary law of interaction between surface elements representing atoms or molecules that build up tubular structures (if the interatomic potential does not have a potential well, the procedures for choosing the optimum scaling functions described in sections 2.2 and 2.3 have to be modified). The tubular potential, therefore, can be parametrized for a diverse range of systems consisting of various types of nano- and microtubular elements, such as nanotubes, nanorods, and microfibers. The common representation of parts of protein molecules as tubes in theoretical investigations of bimolecular conformations and secondary structures<sup>54–56</sup> suggests that, with a proper parametrization, the tubular potential can also be adopted for computational analysis of biological structures.

**Acknowledgment.** Financial support is provided by NASA through the Hypersonics project of the Fundamental Aeronautics program (Award NNX07AC41A) and by the National Science Foundation (Award NIRT-0403876). Computational support is provided by the National Center for Computational Sciences at Oak Ridge National Laboratory (project MAT009).

**Supporting Information Available:** The numerical implementation of the tubular potential in a computer code is discussed in section S1, and the equations for calculation of forces for tubular potential are derived in section S2. Figures S1 and S2 show the domains of functions  $u_{\text{el}}(h, \xi)$  and  $\Phi(h, \zeta)$ , respectively. Figures S3 and S4 illustrate the introduction of local Cartesian coordinates and various geometrical parameters that are used in the calculation of forces acting between nanotubes that interact with each other through the tubular potential. This material is available free of charge via the Internet at <http://pubs.acs.org>.

## References and Notes

- Thess, A.; Lee, R.; Nikolaev, P.; Dai, H.; Petit, P.; Robert, J.; Xu, C.; Lee, Y. H.; Kim, S. G.; Rinzler, A. G.; Colbert, D. T.; Scuseria, G. E.; Tománek, D.; Fischer, J. E.; Smalley, R. E. *Science* **1996**, *273*, 483.
- Rinzler, A. G.; Liu, J.; Dai, H.; Nikolaev, P.; Huffman, C. B.; Rodríguez-Macias, F. J.; Boul, P. J.; Lu, A. H.; Heymann, D.; Colbert, D. T.; Lee, R. S.; Fischer, J. E.; Rao, A. M.; Eklund, P. C.; Smalley, R. E. *Appl. Phys. A* **1998**, *67*, 29.
- Hennrich, F.; Lebedkin, S.; Malik, S.; Tracy, J.; Barczewski, M.; Rösner, H.; Kappes, M. *Phys. Chem. Chem. Phys.* **2002**, *4*, 2273.
- Poulin, P.; Vigolo, B.; Launois, P. *Carbon* **2002**, *40*, 1741.
- Sreekumar, T. V.; Liu, T.; Kumar, S.; Ericson, L. M.; Hauge, R. H.; Smalley, R. E. *Chem. Mater.* **2003**, *15*, 175.
- Berhan, L.; Yi, Y. B.; Sastry, A. M.; Munoz, E.; Selvidge, M.; Baughman, R. J. *Appl. Phys.* **2004**, *95*, 4335.
- Wang, Z.; Liang, Z.; Wang, B.; Zhang, C.; Kramer, L. *Composites, Part A* **2004**, *35*, 1225.
- Wang, S.; Liang, Z.; Pham, G.; Park, Y.-B.; Wang, B.; Zhang, C.; Kramer, L.; Funchess, P. *Nanotechnology* **2007**, *18*, 095708.
- Wang, S.; Liang, Z.; Wang, B.; Zhang, C. *Adv. Mater.* **2007**, *19*, 1257.
- Ma, W.; Song, L.; Yang, R.; Zhang, T.; Zhao, Y.; Sun, L.; Ren, Y.; Liu, D.; Liu, L.; Shen, J.; Zhang, Z.; Xiang, Y.; Zhou, W.; Xie, S. *Nano Lett.* **2007**, *7*, 2307.
- Zhigilei, L. V.; Wei, C.; Srivastava, D. *Phys. Rev. B* **2005**, *71*, 165417.
- Buehler, M. J. *J. Mater. Res.* **2006**, *21*, 2855.
- Leamy, M. J. *Int. J. Solids Struct.* **2007**, *44*, 874.
- Arroyo, M.; Arias, I. *J. Mech. Phys. Solids* **2008**, *56*, 1224.
- Hertel, T.; Walkup, R. E.; Avouris, P. *Phys. Rev. B* **1998**, *58*, 13870.
- Ni, B.; Sinnott, S. B. *Surf. Sci.* **2001**, *487*, 87.
- Qian, D.; Liu, W. K.; Ruoff, R. S. *Compos. Sci. Technol.* **2003**, *63*, 1561.
- Liew, K. M.; Wong, C. H.; Tan, M. J. *Acta Mater.* **2006**, *54*, 225.
- Jeong, B.-W.; Lim, J.-K.; Sinnott, S. B. *J. Appl. Phys.* **2007**, *101*, 084309.
- Girifalco, L. A.; Lad, R. A. *J. Chem. Phys.* **1956**, *25*, 693.
- Stuart, S. J.; Tutein, A. B.; Harrison, J. A. *J. Chem. Phys.* **2000**, *112*, 6472.
- Arroyo, M.; Belytschko, T. *Int. J. Numer. Methods Eng.* **2004**, *59*, 419.
- Arroyo, M.; Belytschko, T. *Meccanica* **2005**, *40*, 455.
- Girifalco, L. A. *J. Phys. Chem.* **1992**, *96*, 858.
- Ruoff, R. S.; Hickman, A. P. *J. Phys. Chem.* **1993**, *97*, 2494.
- Girifalco, L. A.; Hodak, M.; Lee, R. S. *Phys. Rev. B* **2000**, *62*, 13104.
- Sun, C.-H.; Yin, L.-C.; Li, F.; Lu, G.-Q.; Cheng, H.-M. *Chem. Phys. Lett.* **2005**, *403*, 343.
- Sun, C.-H.; Lu, G.-Q.; Cheng, H.-M. *Phys. Rev. B* **2006**, *73*, 195414.
- Stan, G.; Bojan, M. J.; Curtarolo, S.; Gatica, S. M.; Cole, M. W. *Phys. Rev. B* **2000**, *62*, 2173.
- Jiang, L. Y.; Huang, Y.; Jiang, H.; Ravichandran, G.; Gao, H.; Hwang, K. C.; Liu, B. *J. Mech. Phys. Solids* **2006**, *54*, 2436.
- Rey, C.; García-Rodeja, J.; Gallego, L. J.; Alonso, J. A. Clusters and layers of C<sub>60</sub> molecules supported on a graphite substrate. *Phys. Rev. B* **1997**, *55*, 7190.
- Costa, D.; Ruberto, R.; Sciortino, F.; Abramo, M. C.; Caccamo, C. *J. Phys. Chem. B* **2007**, *111*, 10759.
- Liu, H.; Lin, Z.; Zhigilei, L. V.; Reinke, P. *J. Phys. Chem. C* **2008**, *112*, 4687.
- Hodak, M.; Girifalco, L. A. *Chem. Phys. Lett.* **2002**, *363*, 93.
- Sun, C. H.; Li, F.; Liu, C. G.; Lu, G. Q.; Cheng, H. M.; Sun, C. H.; Lu, G. Q. *Appl. Phys. Lett.* **2005**, *86*, 203106.
- Huhtala, M.; Krasheninnikov, A. V.; Aittoniemi, J.; Stuart, S. J.; Nordlund, K.; Kaski, K. *Phys. Rev. B* **2004**, *70*, 045404.
- Nakabayashi, D.; Moreau, A. L. D.; Coluci, V. R.; Galvão, D. S.; Cotta, M. A.; Ugarte, D. *Nano Lett.* **2008**, *8*, 842.
- Garrison, B. J.; Postawa, Z.; Ryan, K. E.; Vickerman, J. C.; Webb, R. P.; Winograd, N. *Anal. Chem.* **2009**, *81*, 2260.
- The cutoff of the nonbonding interaction potential at large distances is not explicitly discussed in ref 21 but is used in the computational code implementing the AIREBO potential and provided to us by Steven Stuart of Clemson University. The values of  $r_c$  and  $r_{c0}$  are from the code.
- Islam, M. F.; Rojas, E.; Bergey, D. M.; Johnson, A. T.; Yodh, A. G. *Nano Lett.* **2003**, *3*, 269.
- Ruoff, R. S.; Tersoff, J.; Lorents, D. C.; Subramoney, Sh.; Chan, Br. *Nature (London)* **1993**, *364*, 514.
- Jiang, Y. Y.; Zhou, W.; Kim, T.; Huang, Y.; Zuo, J. M. *Phys. Rev. B* **2008**, *77*, 153405.
- Srivastava, D.; Menon, M.; Cho, K. *Phys. Rev. Lett.* **1999**, *83*, 2973.
- White, C. T.; Robertson, D. H.; Mintmire, J. W. *Phys. Rev. B* **1993**, *47*, 5485.
- Dresselhaus, M. S.; Dresselhaus, G.; Saito, R. *Carbon* **1995**, *33*, 883.
- Popescu, A.; Woods, L. M.; Bondarev, I. V. *Phys. Rev. B* **2008**, *77*, 115443.
- Marchuk, G. I. *Methods of Numerical Mathematics*, 2nd ed.; Springer-Verlag, New York, 1982.
- Volkov, A. N.; Simov, K. R.; Zhigilei, L. V. Proceedings of the ASME International Mechanical Engineering Congress and Exposition, ASME paper IMECE2008-68021, 2008.
- Volkov, A. N.; Zhigilei, L. V. Manuscript in preparation.
- Volkov, A. N.; Simov, K. R.; Zhigilei, L. V. Proceedings of the 47<sup>th</sup> AIAA Aerospace Sciences Meeting, AIAA paper 2009-1544, 2009.
- Berendsen, H. J. C.; Postma, J. P. M.; van Gunsteren, W. F.; DiNola, A.; Haak, J. R. *J. Chem. Phys.* **1984**, *81*, 3684.
- Teacy, M. M. J.; Ebbesen, T. W.; Gibson, J. M. *Nature* **1996**, *381*, 678.
- Liu, J.; Rinzler, A. G.; Dai, H.; Hafner, J. H.; Bradley, R. K.; Boul, P. J.; Lu, A.; Iverson, T.; Shelimov, K.; Huffman, C. B.; Rodríguez-Macias, F.; Shon, Y.-S.; Lee, T. R.; Colbert, D. T.; Smalley, R. E. *Science* **1998**, *280*, 1253.
- Banavar, J. R.; Hoang, T. X.; Maritan, A.; Seno, F.; Trovato, A. *Phys. Rev. E* **2004**, *70*, 041905.
- Buehler, M. J. *Proc. Natl. Acad. Sci. U.S.A.* **2006**, *103*, 12285.
- Grason, G. M.; Bruinsma, R. F. *Phys. Rev. Lett.* **2007**, *99*, 098101.